NACA RM E54F28

NACA

RESEARCH MEMORANDUM

INVESTIGATION OF A 10-STAGE SUBSONIC AXIAL-FLOW RESEARCH COMPRESSOR

VI - PERFORMANCE EVALUATION AND FLOW DISTRIBUTIONS IN THE FIRST, FIFTH, AND TENTH STAGES

By Ray E. Budinger

Lewis Flight Propulsion Laboratory
Cleveland, Ohio

NATIONAL ADVISORY COMMITTEE FOR AERONAUTICS

WASHINGTON

August 6, 1954
Declassified June 24, 1958

NATIONAL ADVISORY COMMITTEE FOR AERONAUTICS

RESEARCH MEMORANDUM

INVESTIGATION OF A 10-STAGE SUBSONIC AXIAL-FLOW RESEARCH COMPRESSOR VI - PERFORMANCE EVALUATION AND FLOW DISTRIBUTIONS IN THE FIRST, FIFTH, AND TENTH STAGES

By Ray E. Budinger

SUMMARY

The performance and flow distributions in the first, fifth, and tenth stages of a 10-stage axial-flow research compressor were determined at design and part speed in order to study the validity of the compressor design assumptions and to show the effects of part-speed compressor operation on stage performance. The fifth and tenth stages produced design total-pressure ratio at their respective design inlet flow coefficients, whereas the first stage produced less-than-design total-pressure ratio because of overturning by the inlet guide vanes. The correlation of the measured rotor and stator turning angles of the three stages investigated with two-dimensional cascade data indicated that these data are applicable to the design of subsonic multistage axial-flow compressors such as the one investigated herein. The adiabatic efficiencies of the three stages indicated, in general, lower peak values in the first and tenth stages than in the fifth stage, whereas the compressor design assumption utilized a constant value of efficiency for all stages. The tenth stage exhibited the lowest peak efficiency of the three stages investigated.

Design matching of the three stages was not obtained at any one compressor operating condition at design speed. At the operating condition where the fifth and tenth stages were properly matched, the first stage was mismatched because of a combination of inlet-guide-vane overturning and greater-than-design pressure ratio across the second through the fourth stages. The stage matching characteristics of the three stages indicated that neglecting area-correction factors in determining the design area ratios through the compressor was compensated for by the attainment of values of stage efficiency in the intermediate stages that were higher than the assumed design values.

The rotor tip diffusion factor across the fifth rotor exceeded a value of 0.5 with no rapid decrease in element efficiency, which indicates

that this value of rotor-tip diffusion factor apparently would not be applicable as a design limit in the middle stages of this compressor.

The measured axial-velocity distributions at design speed entering the first- and fifth-stage rotors agreed very well with the distributions predicted from the simple radial equilibrium assumption used in the design method except at small regions near the compressor walls. The simple radial equilibrium assumption, however, was inadequate in the prediction of the axial-velocity profile entering the tenth-stage rotor at design speed because of the effect which the large entropy or loss gradient associated with a high hub-tip radius ratio stage has on the axial-velocity distribution. In order to match properly the radial blade elements in the compressor design to obtain optimum stage performance, the losses in the blade-end regions must be known, approximated from boundary-layer loss studies, or taken into account through the use of a suitable radial variation in blade-element efficiency, particularly in the latter stages.

INTRODUCTION

The attainment of design-point performance in a multistage axial-flow compressor is dependent upon the satisfaction of the assumptions required in the compressor design. The purpose of this investigation was to study in a qualitative sense some of the assumptions used in the design procedure reported in reference 1, with particular reference to applicability of two-dimensional low-speed cascade data to multistage compressor design, assumed stage efficiencies, simple radial equilibrium prediction of axial-velocity distributions, and area-correction factors. The evaluation of these assumptions for the present investigation, which was conducted at the NACA Lewis laboratory, was confined to a study of the performance and flow distributions in the first, fifth, and tenth stages of the 10-stage axial-flow research compressor reported in references 1 to 5. These particular stages were chosen for the investigation because the range of operation required of these three stages is representative of the limits of operation of any stage in the compressor. The over-all performance and flow distributions of the first, fifth, and tenth stages are presented for both design and part-speed compressor operation in order to obtain a comparison with the design values and to indicate the effect of part-speed compressor operation on the performance of the individual stages.

It was found in this investigation that the inlet-guide-vane turning was higher than the design value. In a subsequent investigation, the guide vanes were reset to approximate more closely the design flow angles, and the first-stage performance was redetermined. These results are presented in reference 5 and are utilized in the evaluation of first-stage performance presented in this report.

APPARATUS AND INSTRUMENTATION

The 20-inch-tip-diameter, 10-stage axial-flow research compressor reported in references 1 to 5 and schematically shown in figure 1 was used for this investigation. The compressor was designed to produce a total-pressure ratio of 6.45 with an equivalent weight flow of 57.5 pounds per second at an equivalent tip speed of 869 feet per second. The test installation and instrumentation for the determination of the over-all compressor performance are the same as those presented in reference 2.

The design blade and velocity-diagram data for the first, fifth, and tenth stages are given in reference 1. The design blade data are repeated in table I for convenience.

Radial survey instrumentation was located as shown in figure 1 at axial stations 1, 2, and 3 for the first-stage investigation; 9, 10, and 11 for the fifth-stage investigation; and 19, 20, and 22 for the investigation of the tenth stage. These station numbers are consistent with those used in previous investigations of this compressor reported in references 1 to 5. The survey instrumentation at each axial station consisted of a combination claw probe (fig. 2(a)) for measuring flow angle and total pressure and an L-shaped static-pressure wedge (fig. 2(b)). In addition to the survey instrumentation, total temperatures were obtained at the inlet and outlet measuring stations of each of the three stages with a single spike-type radial thermocouple rake (fig. 2(c)). The interstage instrumentation was located circumferentially so that the flow measurements were obtained approximately midway between the leading or trailing edges of adjacent blades in the succeeding or preceding stator row, respectively. The radial measuring stations were located at area centers of equal annular areas. Five radial measuring stations were employed in the investigations of the first and fifth stages, but because of the small passage height (less than 1 in.) in the tenth stage only three radial stations were used.

The radial thermocouple rakes were calibrated over a range of Mach number from 0 to 1.0. The static-pressure probes were calibrated for wall and stem immersion effects over the same range of Mach number.

The radial survey pressure measurements were referenced to wall static-pressure taps at the same axial measuring station on U-tube manometers. The measuring fluids used were water and tetrabromoethane. The total temperature at each radial station was measured differentially with the total temperature at axial station 0 on a self-balancing calibrated potentiometer.

PROCEDURE

The investigation of the first, fifth, and tenth stages was separated into three phases in order to simplify the interstage instrumentation problem. At each selected compressor operating point, differential stage temperatures were obtained at the inlet and exit of the stage along with simultaneous surveys of flow angle, total pressure, and static pressure at the inlet and exit of the rotor and the exit of the stage. After the stage had been investigated over a range of weight flow at speeds from 50 to 100 percent of design, the interstage instrumentation was removed and reinstalled on the next stage chosen for investigation. The process was repeated until the performance of each of the three stages had been determined over the compressor performance map. The compressor-inlet conditions at each speed were varied in order to obtain a Reynolds number of approximately 0.2×10^6 relative to the first rotor at the tip. The over-all compressor performance data are presented in figure 3 to indicate the range of weight flow and speed investigated. These data were evaluated from a calculated discharge total pressure obtained from the average discharge wall static pressure, total temperature, and orifice weight flow with use of the method recommended in reference 6.

The total-pressure ratio and adiabatic temperature-rise efficiency of the three stages investigated were determined from arithmetic averages of the total pressures and total temperatures at the rotor-inlet and stator-discharge measuring stations. Because no measurements were obtained after the tenth-stage stator row, the evaluation of the tenth-stage performance includes the total-pressure loss across the exit guide vanes. The stage performance is presented in terms of equivalent total-pressure ratio plotted against inlet flow coefficient or the ratio of mean axial velocity to wheel speed, which results in a single performance curve that is essentially independent of speed. These stage performance parameters are derived in reference 7 and are used in the following form in this report:

Flow coefficient:

$$\frac{Q}{U_t A_i} = \frac{WRT_i}{U_t A_i P_i} \left(1 + \frac{\gamma - 1}{2} M_i^2\right)^{\frac{1}{\gamma - 1}} \qquad (1)$$

(All symbols are defined in the appendix.) The Mach number in equation (1) was determined from a ratio of the average total and static pressures obtained from survey measurements.

Equivalent total-pressure ratio:

$$(P_o/P_i)_e = (Y_e + 1.0)^{\frac{\gamma}{\gamma-1}} \quad (2)$$

where

$$Y_e = K \frac{\Delta H_{is}}{U_t^2}$$

and

$$K = (U_t/\sqrt{T_i})_d^2 \frac{1}{c_p}$$

STAGE OVER-ALL PERFORMANCE CHARACTERISTICS

The over-all performance in terms of the previously discussed parameters is presented for the first, fifth, and tenth stages in figures 4(a), (b), and (c), respectively. The stage design points are shown for comparison. At the design inlet flow coefficient to the first, fifth, and tenth stages, the equivalent total-pressure ratio was 1.08, 1.21, and 1.23 compared with the design values of 1.145, 1.205, and 1.240, respectively. The peak efficiency of all three stages occurred at lower-than-design flow coefficient and very nearly coincided with the maximum total-pressure-ratio flow point of each stage. The fact that peak stage efficiency occurred at a stage flow coefficient lower than design might be expected, because the compressor blading was selected for approximately minimum loss and not maximum lift-drag ratio, which occurs at a higher angle of attack and hence at a lower flow coefficient than design. The peak efficiencies obtained were approximately 0.89, 0.94, and 0.83 for the first, fifth, and tenth stages, respectively. It should be noted that the tenth stage has been penalized for any loss across the exit guide vanes, and consequently the total-pressure ratio and efficiency of this stage as defined by a rotor and single stator row would probably be slightly higher. However, the low efficiency of the tenth stage may also be partially attributed to the inherent high losses associated with exit stages of high hub-tip radius ratio and low aspect ratio.

The equivalent total-pressure-ratio curves shown in figure 4 indicate that at the design stage-inlet flow condition the fifth and tenth stages produce very close to design stage total-pressure ratio, while the first stage produces less than design stage total-pressure ratio. The low inlet-stage total-pressure ratio obtained at design inlet flow coefficient can be attributed to an inlet-guide-vane turning greater than design. A subsequent investigation in which the

guide-vane setting with respect to the compressor axis was reduced by 5° to compensate for the approximately constant 4° overturning along the radius is reported in reference 5. The first-stage performance determined with the design guide-vane turning is compared with that obtained in this investigation and with the stage design point in figure 5. The equivalent total-pressure ratio of the first stage at the design inlet flow coefficient was increased to a value of 1.16 with the reset guide vanes, as compared with the design value of 1.145. This comparison indicates the importance of accurately predicting the inlet flow angle (stator discharge angle) to the rotor, particularly for large values of flow angle, in order to obtain design angle of attack at design inlet flow coefficient for the individual stages.

The importance of accurately predicting the stator discharge angle may also be seen from a consideration of the following equation, which expresses the stage-inlet flow coefficient in terms of the relative and absolute inlet flow angles to the rotor:

$$UA_i/Q = \tan \beta_i' + \tan \beta_i \qquad (3)$$

In order to obtain design angle of attack on the rotor, which corresponds to design relative inlet flow angle β_i', any error in absolute flow angle β_i must be accompanied by a change in flow coefficient. The change in flow coefficient in turn alters the rotor velocity diagram so that the work input to the stage must also change. In summary, a stator discharge angle that is too high will displace the stage performance curve toward lower values of flow coefficient and total-pressure ratio as shown in figure 5, while the converse would be true for stator discharge angles lower than design.

STAGE MATCHING CHARACTERISTICS

Design-point over-all compressor performance not only necessitates the attainment of design-point performance of the individual stages but also requires the proper matching of the stage design points at a specific compressor-inlet weight flow. The proper matching of the stages at design speed is determined by the flow coefficient or the mean axial velocity entering each stage. Since the axial velocity must satisfy continuity, the stage matching is determined by the effective area and density ratios at the entrance to each stage. The effective area ratio is obtained through the use of area-correction factors to account for boundary-layer displacement thickness and area blockage due to blade wakes, while the density ratio is dependent upon the assumed stage efficiencies and the stage energy addition. Consequently, the design matching of the individual stages is largely dependent upon the validity of the design assumptions as corroborated by experimental information.

The aerodynamic design of this compressor (ref. 1) utilized an assumed polytropic stage efficiency of 0.90 for all stages in the compressor. The corresponding design stage adiabatic efficiency would be only slightly less than this value because of the small pressure rise obtained across a single stage. The adiabatic temperature-rise efficiency data presented in figure 4 indicate in a relative sense that the first- and tenth-stage peak efficiencies are somewhat lower than the values obtained in the fifth stage, with the tenth stage exhibiting the lowest peak efficiency of the three. This efficiency trend is in contrast to the design assumption previously stated which utilized a constant value of efficiency for all stages.

The aerodynamic design also made no allowance for boundary-layer or area blockage because of the lack of information available at the time of the design. Neglecting the effects of area blockage in the compressor design would affect the stage matching so that each successive stage would be forced to operate at flow coefficients that are increasingly higher than the design values. The solid design-speed symbols shown in figure 4 indicate the relative matching of the three stages at a given compressor operating point (point A, fig. 3). The lower-than-design flow coefficient to the fifth stage (point A, fig. 4(b)) at approximately design inlet flow coefficient to the first stage (point A, fig. 4(a)) indicates that the low total-pressure ratio obtained across the first stage and the design area-ratio variation, both of which tend to increase the flow coefficient, must be compensated for by a combination of higher-than-design energy addition and efficiency of the stages between the first and the fifth. This fact is substantiated by the over-all performance investigation (ref. 2) and the individual stage performance investigation (ref. 4), both of which indicated higher-than-design loading of the second, third, and fourth stages. The reason for the increased loading in the second through the fourth stages contradicts the trend that would be expected, and consequently an explanation would require further experimental information on the stages involved. The flow coefficient entering the tenth stage at point A on figure 4(c) is considerably lower than the design value. This low flow coefficient is caused by the higher-than-design energy addition of the preceding stages, which successively reduced the flow coefficient entering the tenth stage to the value indicated.

The design-speed data points B on figures 4(b) and (c) coincide with the design inlet flow coefficient to the fifth and tenth stages, respectively, and are obtained at approximately the same over-all compressor pressure ratio as shown by point B in figure 3. At this point the first stage is also obviously operating very near design flow coefficient. However, because of the guide-vane overturning, the total-pressure ratio and efficiency are both lower than design, causing this stage to be mismatched with the fifth and tenth stages with respect

to pressure ratio. The attainment of design stage flow coefficient and design stage total-pressure ratio at a single compressor operating condition at design speed indicates that design matching of the fifth and tenth stages was actually obtained. Since design matching of the fifth and tenth stages was obtained, the area-correction factors that were neglected in the design must have been compensated for by the attainment of higher than the assumed value of design stage efficiency in the intermediate stages.

STAGE FLOW DISTRIBUTIONS AND ELEMENT PERFORMANCE

The previous discussion has presented the stage performance on the basis of the average flow conditions entering and leaving the stages. In order to study the performance of the individual stages more thoroughly, it is necessary to present the radial distributions of flow entering each stage and the resultant element performance obtained. In the following sections the inlet flow distributions and the element performance across each of the three stages investigated are presented at three compressor operating points. The three points selected correspond to approximately peak over-all compressor efficiency at 50, 80, and 100 percent of design speed. These points were chosen in order to present a comparison with the design flow distribution at design and part speed and also to indicate the relative matching of the flow distributions in the three stages at a given compressor-inlet weight flow. The three points chosen for further study of the first, fifth, and tenth stages are designated by solid symbols on the figures. The design-speed point is the point A discussed in the preceding section.

First Stage

Inlet flow distributions. - The radial variation of flow conditions entering the first rotor row is presented in figure 6 as plots of absolute flow angle, axial velocity to tip speed ratio, angle of attack, and relative inlet Mach number at the three selected compressor operating conditions designated by the solid symbols in figure 3. The design radial variations obtained from the tables of reference 1 are also shown in figure 6. The absolute flow angles entering the first rotor are higher than design at all speeds (fig. 6(a)) because of the aforementioned overturning by the inlet guide vanes. The rapid increase in magnitude of the flow angles in the tip region at the low-speed operating condition (50 percent of design speed) indicates the presence of a stall of the tip section of the first rotor. Hot-wire-anemometer traces obtained on the subject compressor, which are presented in reference 3, indicate the presence of rotating stall in the tip region of the first stage at 50 percent of design speed. The flow-angle measurements, therefore,

indicate a correlation between blade stall obtained from flow measurements and rotating stall as determined by hot-wire anemometers.

The axial-velocity distribution shown in figure 6(a) at design speed indicates good agreement with the design radial variation except in the blade end regions. The design radial distribution was determined through the use of the assumption that simple radial equilibrium of pressures and centrifugal forces is satisfied after each blade row. An analysis of radial equilibrium applied to the data obtained on a number of compressors including this 10-stage compressor and presented in reference 8 indicates that simple radial equilibrium is a good assumption after the inlet guide vanes, provided that passage curvature and free-stream entropy gradients are small. The high absolute flow angles (fig. 6(a)), when combined with the axial-velocity distribution entering the first rotor at the design-speed operating condition, which is point A on figure 4(a), result in lower-than-design angle of attack and relative inlet Mach number on the first rotor, as shown in figure 6(b). The low angle of attack and relative inlet Mach number both tend to decrease the first-stage energy addition and total-pressure ratio below the design value. Because the compressor operates over a very small range of inlet weight flow at design speed (fig. 3), the first rotor will always operate at lower-than-design angle of attack and total-pressure ratio at design speed, as indicated in figure 4(a).

Rotor turning angles. - The variation of rotor turning angle with angle of attack at five radial positions is presented in figure 7 for all flow conditions investigated. The design rotor turning angle obtained from reference 1 and the turning-angle variation predicted from the data of reference 9 are also shown. The end points of the dashed line do not represent a two-dimensional prediction of blade stall but rather represent the limits of interpolation and extrapolation of the cascade data of reference 9. Since these cascade data were not available at the time of the compressor design, the design rotor turning angles shown in figure 7 were obtained from available low-speed cascade data presented in chart form in reference 1. The agreement of these data with those of reference 9 indicates that the charts of reference 1 could be applied to compressor designs employing 65-series 10-percent-thick blades within the same range of camber, solidity, and relative inlet flow angles as the design of the subject compressor.

The cascade data are determined for constant axial velocity across the blade elements; however, in the compressor, the axial-velocity distribution does not remain fixed. The measured angle of attack and turning angle can be approximately corrected for this effect by using an equivalent velocity diagram. This equivalent diagram is formed by using the mean value of the entering and leaving axial velocity for a given blade element and the measured tangential velocity. A comparison at the design-speed operating point (point A) is made in table II between

the measured and equivalent values of angle of attack and turning angle for the rotors and stators of the three stages investigated. From table II, it can be seen that the angle of attack and turning angle, when calculated on the equivalent basis, change in the same direction; consequently, little improvement in the correlation with the cascade data of reference 9 could be obtained. For this reason and because the equivalent diagram masks the effects of axial-velocity changes across a blade row, only the measured values of angle of attack and turning angle are presented.

The tailed symbols in figure 7 indicate the data points obtained in the range of compressor operation affected by rotating stall. This range was determined from the results of reference 3, which indicated the presence of rotating stall for all flow conditions at 50 and 60 percent of design speed and for all equivalent inlet weight flows below approximately 30 pounds per second at 70 percent of design speed. The data obtained by time-averaging instruments are questionable in this region because of the pulsating nature of the flow and are presented only for the sake of completeness.

The estimated accuracy of the measured flow angles is approximately $\pm 1\frac{1}{2}^{\circ}$. The relative flow angles, however, are also dependent on the measured velocities, and consequently the rotor angles of attack and turning angles may be in greater error than the absolute flow angles. In view of these limitations, the agreement between the measured rotor turning angles with the two-dimensional cascade data (fig. 7) is considered good at all radii. The trend of the experimental rotor turning angle data, in general, parallels the interpolated cascade data at all radial positions with the absolute values of turning angle being somewhat higher than predicted at the outer radii. The curves show that design angle of attack on all blade elements of the first rotor occurs in the flow range obtained at 90 percent of design speed. The design-speed data points on figure 7 fall below design angle of attack at all radial positions. The lower-than-design angle of attack is in agreement with the stage performance data discussed previously and results from inlet-guide-vane overturning.

Stator turning angles. - The variation of first-stage stator turning angle with angle of attack is shown in figure 8 at five radial positions. The data points affected by rotating stall are designated by tailed symbols at each radial position. Excluding these points, the first stator operates over a very narrow range of angle of attack in comparison with the first rotor on all blade elements except the tip element (fig. 8(a)). Design angle of attack occurs in the flow range obtained at design speed on all elements. However, at design angle of attack the observed stator turning angles appear to be slightly low but in general agree fairly well with the cascade prediction.

The combined effect of the low stator turning and the excessive guide-vane turning would be to decrease the angle of attack on the succeeding rotor. The lower-than-design density ratio across the first stage will increase the axial velocity entering the second stage and also tend to decrease the angle of attack entering the second rotor row. The individual stage performance investigation (ref. 4), however, shows that the second-stage total-pressure ratio was slightly higher than the design value (1.18 compared with the design value of 1.16) at design and higher-than-design flow coefficients. The explanation for this apparent inconsistency between the angle-of-attack trend and second-stage total-pressure ratio is beyond the scope of the subject report, since complete radial surveys such as those obtained for the first, fifth, and tenth stages would be required.

Element performance. - The element performance across the first stage is presented in terms of adiabatic temperature-rise efficiency and dimensionless temperature-rise coefficient in figure 9 at the three points designated by solid symbols in figures 3 and 4(a). The radial distribution of efficiency indicates that the element efficiencies in the hub region remain relatively constant over a wide range of compressor operating conditions, whereas the tip-element efficiencies are extremely sensitive to changes in compressor operating conditions. Consequently, the peak efficiency of the first stage appears to be uniquely determined by the angle of attack entering the first-stage rotor in the tip region.

The low efficiency of the first stage at design speed shown in figure 4(a) appears to be caused by the very low efficiency of the tip elements of this stage, as indicated in figure 9. The diffusion factor, a blade-loading parameter developed in reference 10 that correlates single-stage blade-element efficiency data, is presented for the first-stage rotor at design speed in figure 10. The calculated design values are also shown. The results of reference 10 indicate that the blade-element efficiency at optimum incidence in the tip region decreases rapidly at diffusion factors above 0.5. The first-stage rotor appears to operate significantly below this value in the tip region as shown in figure 10, thus probably eliminating this factor as a cause of the low tip-element efficiency, even though the first rotor is operating below optimum incidence in the tip region at this particular operating point. The low tip-element efficiencies could possibly be attributed to separation of the flow from the blade pressure surface caused by a combination of low angle of attack and high relative inlet Mach number to the first rotor at design speed. The angle of attack and relative inlet Mach number shown in figure 6(b) in the tip region, however, appear to be in the low-loss region for this blade section, as shown in reference 9. Nevertheless, it is felt that local disturbances may be instigating separation and associated high losses, thus causing the low tip-element efficiencies.

The dimensionless temperature-rise coefficient, which is a measure of the actual energy addition to the compressor, increases with decreasing speed (fig. 9) primarily because of the increased angle of attack on the first rotor as shown in figure 6(b). At design speed the average value of the energy addition (fig. 9) was lower than the design value as a result of the lower-than-design angle of attack on the first-stage rotor.

The effect of the lower-than-design energy addition and efficiency (fig. 9) on the axial velocity leaving the rotor is indicated in figure 10. The low density ratio across the first-stage rotor at design speed resulted in an increase in axial velocity across the entire flow passage in order to satisfy continuity after the rotor. A part of this axial-velocity increase may be attributed to effective area reduction caused by boundary-layer growth along the compressor walls, which was not accounted for in determining the design area ratios.

Fifth Stage

Inlet flow distributions. - The flow distributions at the entrance to the fifth rotor are presented in figure 11 at the compressor operating points designated by the solid symbols in figure 3. At the peak compressor efficiency point at design speed (point A, fig. 4(b)), the flow conditions entering the fifth stage match the design variations very closely except in the blade end regions (fig. 11). The low axial velocity in these regions (fig. 11(a)) will reduce the mean axial velocity and hence the stage-inlet flow coefficient below the design value. Because the design flow distributions entering the fifth stage are obtained over the main portion of the passage height at a reduced flow coefficient, design performance of this stage would not be obtained at the over-all compressor design point. In order to obtain design performance of the middle stage of the compressor at the over-all compressor design point, it would be necessary to know the losses in the blade end regions and incorporate this knowledge in the design by a method such as that presented in reference 8. The simple design method used in reference 1, however, is fairly adequate in the prediction of the axial-velocity distribution across the main portion of the passage height at this point in the compressor.

The corresponding flow conditions entering the fifth rotor at the lower compressor speeds (50 and 80 percent of design) shown in figure 11 show the extent to which the upstream flow disturbances introduced in the inlet stages have dissipated in reaching the fifth stage. The increase in angle of attack in the tip region and decrease in axial velocity at 50 percent of design speed indicate that the stall condition in the first stage is affecting the performance of at least the next four stages. This fact is corroborated by the hot-wire-anemometer data of

reference 3, which indicated that the flow fluctuations caused by rotating stall were very noticeable through the first five stages and then diminished quite rapidly.

Rotor turning angles. - The fifth-rotor turning angles are plotted against angle of attack at five radial positions in figure 12 for all flow conditions investigated. The design rotor turning angle and the two-dimensional cascade predicted turning angles (ref. 9) are shown for comparison. The observed data are subject to the same sources of error as imposed on the first-stage data. In addition, all the upstream disturbances generated by the preceding four stages may affect the downstream measurement so that considerable scatter of data points may be expected over the range of speed and flow investigated. The data points that may be affected by rotating stall are indicated by tailed symbols in figure 12. The data points at all speeds overlap, since approximately the same range of flow coefficient and hence of angle of attack (figs. 4(b) and 12) is obtained in the middle stage of the compressor over the range of speed investigated. As shown in figure 12, the angle-of-attack range on all blade elements of the fifth rotor is approximately 10° excluding the lowest speed in the tip region.

In view of these facts and the fact that the scale factor for the fifth-rotor turning angles (fig. 12) is $2\frac{1}{2}$ times that for the first-rotor turning angles (fig. 7), the data correlate design and predicted values reasonably well, although the observed values are slightly low.

Stator turning angles. - The fifth-stator turning angles are presented in figure 13. The major portion of the data shown in figure 13, excluding those points affected by rotating stall, agree with the two-dimensional cascade prediction within the experimental accuracy of the data. In the tip region (fig. 13(a)), the very high angles of attack are probably caused by the low axial velocities entering the fifth rotor (fig. 11(a)). At design equivalent speed, design angle of attack and predicted turning angles were obtained on all blade elements of the fifth stator except at the tip (fig. 13).

Element performance. - The stage element efficiency variation and dimensionless temperature-rise coefficient are presented for the fifth stage in figure 14 at the three points designated by solid symbols in figures 3 and 4(b). The blade-element efficiencies indicate a general trend toward increasing efficiency with increasing speed at the peak over-all compressor efficiency operating points. The diffusion factor across the fifth rotor at design speed (fig. 15) exceeds the value of 0.5 in the tip region designated in reference 10 as the value above which the tip-element efficiencies decrease rapidly. Since the element efficiency in the tip region remains high (fig. 14), it appears that this value of diffusion factor apparently would not be applicable as a design limit in the middle stage of this compressor. The calculated design values of diffusion factor are also shown in figure 15.

The dimensionless temperature-rise coefficient across the fifth stage (fig. 14) in general follows the same trend as that found for the angle of attack entering the fifth rotor (fig. 11(b)). At design speed the dimensionless temperature-rise coefficient or energy addition was higher than the design value across the entire blade passage, even though design angle of attack was obtained over most of the passage as shown in figure 11(b). Since the rotor turning angles were slightly low (fig. 12), the higher-than-design energy addition must be attributed to the axial-velocity change across the rotor. The axial-velocity ratio across the fifth rotor at design speed is presented in figure 15. The data indicate that the axial velocity decreased across the fifth rotor so that the observed value of this ratio was less than the design value at all radii. These low axial velocities at the exit of the fifth rotor, when combined with the high element efficiencies of this stage, produced greater-than-design dimensionless temperature-rise coefficients and total-pressure ratios, as shown in figures 14 and 4(b) (point A). The low axial velocity leaving the fifth rotor and the higher-than-design density rise across the fifth stage will increase the angle of attack on succeeding stages so that at this particular compressor operating point the exit stages will operate at lower-than-design flow coefficient and therefore will be mismatched with the front and middle stages.

Tenth Stage

Inlet flow distributions. - The inlet flow distributions to the tenth stage are presented in figure 16 at the compressor operating points designated by the solid symbols in figure 3. The absolute flow angles entering the tenth rotor agree fairly closely with the design values. The velocities at all speeds show a tendency to decrease in the hub and tip regions, as shown in figure 16. This deviation from the nearly linear design axial-velocity distribution can be attributed to the fact that this is a very high hub-tip radius ratio stage ($z_{h,19} = 0.91$), and consequently the losses that tend to accumulate in the blade end regions in passing through the compressor will seriously affect the radial flow distributions. The radial extent of these losses increases considerably as a percentage of passage height in the tenth stage, as evidenced by a comparison of the axial-velocity distributions entering the fifth and tenth rotors (figs. 11(a) and 16(a)).

The design distribution of axial velocity was determined from a consideration of simple radial equilibrium; however, the measured data indicate the inadequacy of this design assumption in predicting the axial-velocity profile in the tenth stage of this compressor. The radial equilibrium analysis of the flow entering the tenth rotor presented in reference 8 indicates that the deviation of the measured axial-velocity distribution from the simple radial equilibrium prediction using measured flow angle and total energy gradient is due almost entirely to the entropy or loss gradient across the passage.

A reproduction of figure 27(a) of reference 8 is presented in figure 17 to show a comparison of the observed axial-velocity distribution with those computed by assuming simple radial equilibrium and simple radial equilibrium including entropy gradient. The deviation in shape of the simple radial equilibrium prediction of axial-velocity ratio from the design distribution, which also utilized the simple radial equilibrium assumption, is due to the fact that the measured flow angle distribution did not agree exactly with the design flow angles (fig. 16(a)) and also to the fact that the measured total energy gradient entering the tenth rotor was not constant from hub to tip, as established in the design method. Since the deviation from design absolute flow angle is relatively small, the difference in these two curves primarily indicates the effect of inconstant total energy on the axial-velocity distribution. Since the absolute flow angle can be predicted reasonably well from the two-dimensional cascade data and since the total energy gradient is usually prescribed in the design, the axial-velocity distribution could be more accurately predicted if the losses in the blade end regions were known. This again would require a knowledge of the flow in the boundary layer or might be more easily taken into account through the use of a suitable assumption of a radial variation of blade-element efficiency.

The lower-than-design axial velocity and hence flow coefficient obtained at design speed, as shown in figures 16(a) and 4(c) (point A) may be attributed to a higher-than-design density at the entrance to the tenth stage. The analysis of the fifth-stage performance at the peak compressor efficiency point at design speed indicated a higher stage loading and efficiency and hence higher-than-design density in the latter stages of the compressor. As a result of the low axial velocity, the angle of attack at the tenth-stage rotor (fig. 16(b)) at the design-speed operating point is considerably higher than the design values, particularly in the hub region. The angle-of-attack distribution at peak over-all compressor efficiency at 50-percent speed is very uniform and well above the high-loss region of operation where negative blade stall would be encountered. Consequently, it can be seen that this particular compressor is not penalized by windmilling of the exit stages even at the low speeds investigated, as shown by the pressure rise obtained across the tenth stage in figure 4(c) at these speeds.

Rotor turning angles. - The tenth-rotor turning angles shown in figure 18 at three radial positions for all flow conditions investigated agree very well with the design values and with the cascade prediction of reference 9. These data indicate that the blade hub section of the tenth rotor operates over the widest range of angle of attack, in contrast to the operation of the first rotor, which experienced a much wider range of angle of attack in the tip region, as shown in figure 7. The blade tip sections of the inlet stages appeared to initiate rotating stall at low compressor speeds (ref. 3). However, because the flow is probably very nearly two-dimensional in high hub-tip radius ratio exit

stages, it is felt that stall of the blade hub section or of any blade section of the tenth stage will cause complete stall of the blade row and will result in surge of the compressor when operating at high speeds.

Because of the wide range of angle of attack obtained at the tenth rotor between choke and surge weight flow at each speed, this rotor will operate close to design angle of attack at some flow condition at each speed investigated. As a result, this stage operates close to peak efficiency near surge at low speeds (fig. 4(c)) and tends to compensate for the low efficiency of the inlet stage indicated in figure 4(a), thus tending to maintain high peak compressor efficiency at part speed as shown in figure 3.

Element performance. - The dimensionless temperature-rise coefficient obtained across the tenth stage is presented in figure 19 at the three points designated by solid symbols in figures 3 and 4(c). The radial variation of element efficiency across the tenth stage is not presented because of the inconsistency of the total-pressure measurements obtained after the exit guide vanes. This inconsistency was probably caused by the effects of the wakes of two successive rows of stator blades on the measuring instrument. Efficiencies calculated by use of circumferential averages of total pressure obtained from compressor-discharge total-pressure rakes indicated low efficiency at the hub measuring station and increasing element efficiencies toward the tip at the design-speed operating point (point A, fig. 4(c)). The low efficiency of the tenth stage near the hub at design speed may be attributed to an increase in blade losses caused by the high angle of attack entering the tenth rotor in the hub region. The diffusion factor calculated across the tenth rotor at design speed is shown in figure 20 in order to indicate the magnitude of this blade-loading parameter in the tenth stage of this compressor in comparison with the calculated design value. It should be noted that the tenth rotor operates at higher than optimum incidence at this point, and hence the values of measured diffusion factor are not too significant.

The observed dimensionless temperature-rise coefficient at design speed (fig. 19) is considerably higher than the design distribution, because the tenth stage is operating at lower-than-design flow coefficient, as shown by point A in figure 4(c), and consequently at higher-than-design angle of attack as shown in figure 16(b). The measured dimensionless temperature-rise coefficient or energy addition at design speed does not follow the trend toward very high energy input in the hub region, which is indicated by the high angle of attack in this region. The deviation of the observed energy-addition variation from the angle-of-attack distribution in the hub region can be attributed to the axial-velocity change across the tenth rotor, which is shown in figure 20. The large increase in axial velocity in the hub region decreases the energy addition so that the effect of the high angle of attack on the energy addition is cancelled. The greater-than-design axial-velocity increase across the entire passage will also tend to decrease

the peak total-pressure ratio attainable from the tenth stage. As shown in figure 4(c), the peak total-pressure ratio is only slightly greater than the design value.

SUMMARY OF RESULTS

The results of an investigation of the performance and flow distributions in the first, fifth, and tenth stages of a 10-stage axial-flow research compressor may be summarized as follows:

1. Design total-pressure ratio was obtained across the fifth and tenth stages at their respective design inlet flow coefficients. The first stage produced less than design total-pressure ratio at its design inlet flow coefficient because of overturning by the inlet guide vanes.

2. The peak adiabatic efficiencies of the three stages indicated higher efficiency in the fifth stage than in the first and tenth stages, whereas the design assumption utilized a constant value of efficiency for all stages. The tenth stage was the least efficient of the three stages investigated.

3. The two-dimensional low-speed cascade data predicted the stator discharge angles and rotor turning angles in the three representative stages investigated with reasonable accuracy, thus indicating the applicability of the cascade data to the design of subsonic multistage axial-flow compressors.

4. Design matching of the three stages investigated was not obtained at any one compressor operating condition at design speed. At the operating condition where the fifth and tenth stages were properly matched, the first stage was mismatched because of a combination of inlet-guide-vane overturning and greater-than-design pressure ratio across the second through the fourth stages.

5. The stage matching characteristics of the three stages investigated indicated that neglecting area-correction factors in determining the design area ratios through the compressor was compensated for by the attainment of higher than the assumed design values of stage efficiency in the intermediate stages.

6. The diffusion factor in the tip region of the fifth rotor exceeded the value of 0.5 previously designated as the value above which tip-element efficiencies decrease rapidly. Since the element efficiency in the tip region remained high, this value of diffusion factor apparently would not be applicable as a design limit in the middle stage of this compressor.

7. The measured axial-velocity distributions at design speed entering the first- and fifth-stage rotors agreed very well with the distributions predicted from the simple radial equilibrium assumption used in the design method, except at small regions near the compressor walls. The simple radial equilibrium assumption, however, was inadequate in the prediction of the axial-velocity profile entering the tenth-stage rotor at design speed because of the effect which the large entropy or loss gradient associated with a high hub-tip radius ratio stage has on the axial-velocity distribution.

Lewis Flight Propulsion Laboratory
National Advisory Committee for Aeronautics
Cleveland, Ohio, June 23, 1954

APPENDIX - SYMBOLS

The following symbols are used in this report:

A	annulus area, sq ft
c_p	specific heat at constant pressure, Btu/(lb)($^\circ$F)
D	diffusion factor
g	acceleration due to gravity, ft/sec^2
ΔH	change in total enthalpy, Btu/lb
J	mechanical equivalent of heat, ft-lb/Btu
M	Mach number
P	total pressure, lb/sq ft
Q	volume flow, cu ft/sec
R	gas constant, ft-lb/(lb)($^\circ$F)
T	total temperature, $^\circ$R
U	wheel speed, ft/sec
V_a	axial velocity, ft/sec
W	weight flow, lb/sec
Y	pressure-ratio function, $(P_o/P_i)^{\frac{\gamma-1}{\gamma}} - 1.0$
z	radius ratio
α	angle of attack, deg
β	air angle, angle between compressor axis and air velocity, deg
$\Delta\beta$	turning angle, deg
γ	ratio of specific heats
δ	ratio of total pressure to standard sea-level pressure

η adiabatic temperature-rise efficiency

θ ratio of total temperature to standard sea-level temperature

Subscripts:

d design conditions

e equivalent, indicates that the parameter to which it is affixed has been corrected to design speed

h hub

i stage inlet

is isentropic

m mean

o stage outlet

t tip

0 inlet depression tank

1,9,19 entrance measuring station to first-, fifth-, and tenth-stage rotors, respectively

2,10,20 discharge measuring station from first-, fifth-, and tenth-stage rotors, respectively

3,11 discharge measuring station from first- and fifth-stage stators, respectively

22 measuring station at discharge of exit guide vanes

Superscripts:

' relative to rotor blade row

REFERENCES

1. Johnsen, Irving A.: Investigation of a 10-Stage Subsonic Axial-Flow Research Compressor. I - Aerodynamic Design. NACA RM E52B18, 1952.

2. Budinger, Ray E., and Thomson, Arthur R.: Investigation of a 10-Stage Subsonic Axial-Flow Research Compressor. II - Preliminary Analysis of Over-All Performance. NACA RM E52C04, 1952.

3. Huppert, Merle C., Costilow, Eleanor L., and Budinger, Ray E.: Investigation of a 10-Stage Subsonic Axial-Flow Research Compressor. III - Investigation of Rotating Stall, Blade Vibration, and Surge at Low and Intermediate Compressor Speeds. NACA RM E53C19, 1953.

4. Budinger, Ray E., and Serovy, George K.: Investigation of a 10-Stage Subsonic Axial-Flow Research Compressor. IV - Individual Stage Performance Characteristics. NACA RM E53C11, 1953.

5. Budinger, Ray E., and Serovy, George K.: Investigation of a 10-Stage Subsonic Axial-Flow Research Compressor. V - Effect of Reducing Inlet-Guide-Vane Turning on Over-All and Inlet-Stage Performance. NACA RM E53H10, 1954.

6. NACA Subcommittee on Compressors: Standard Procedure for Rating and Testing Multistage Axial-Flow Compressors. NACA TN 1138, 1946.

7. Medeiros, Arthur A., Benser, William A., and Hatch, James E.: Analysis of Off-Design Performance of a 16-Stage Axial-Flow Compressor with Various Blade Modifications. NACA RM E52L03, 1953.

8. Hatch, James E., Giamati, Charles C., and Jackson, Robert J.: Application of Radial-Equilibrium Condition to Axial-Flow Turbomachine Design Including Consideration of Change of Entropy with Radius Downstream of Blade Row. NACA RM E54A20, 1954.

9. Herrig, L. Joseph, Emery, James C., and Erwin, John R.: Systematic Two-Dimensional Cascade Tests of NACA 65-Series Compressor Blades at Low Speeds. NACA RM L51G31, 1951.

10. Lieblein, Seymour, Schwenk, Francis C., and Broderick, Robert L.: Diffusion Factor for Estimating Losses and Limiting Blade Loadings in Axial-Flow Compressor Blade Elements. NACA RM E53D01, 1953.

TABLE I. - BLADE DATA

Stage	Blade	Hub radius at entrance, in.	Number of blades	Blade chord, in.	Design camber	Maximum thickness, percent of chord
1	Rotor	5.500	25	1.550	0.91	10
1	Stator	5.822	27	1.550	.91	10
5	Rotor	7.639	37	1.380	1.12	10
5	Stator	7.838	39	1.380	1.12	10
10	Rotor	9.085	56	1.120	1.30	10

TABLE II. - COMPARISON OF MEASURED AND EQUIVALENT VALUES OF ANGLE OF ATTACK AND TURNING ANGLE AT DESIGN SPEED (point A)

Stage	Rotor					Stator				
	z	α	α_e	$\Delta\beta'$	$\Delta\beta'_e$	z	α	α_e	$\Delta\beta$	$\Delta\beta_e$
1	0.96	4.1	3.7	11.6	10.9	0.97	8.2	9.9	9.1	12.4
	.89	4.2	3.1	13.2	11.2	.90	9.7	11.0	11.0	13.5
	.81	5.9	4.7	16.4	14.5	.82	12.1	12.8	14.8	16.1
	.71	8.6	7.1	16.4	14.2	.73	11.4	12.3	12.3	13.8
	.61	12.4	10.5	20.3	17.7	.64	14.2	14.7	15.2	16.0
5	0.98	20.2	22.1	14.2	18.1	0.98	23.6	20.2	24.3	18.2
	.93	14.0	14.9	15.3	17.0	.94	15.4	14.6	20.3	18.9
	.89	14.6	15.2	17.6	18.6	.90	15.4	14.8	20.2	19.0
	.84	14.9	15.3	17.6	18.2	.85	14.8	14.8	20.9	20.9
	.79	19.5	19.8	20.8	21.4	.81	16.3	16.5	23.0	23.4
10	0.98	21.2	20.4	24.1	23.8					
	.95	24.0	22.4	27.4	26.7					
	.92	31.1	26.3	37.4	34.8					

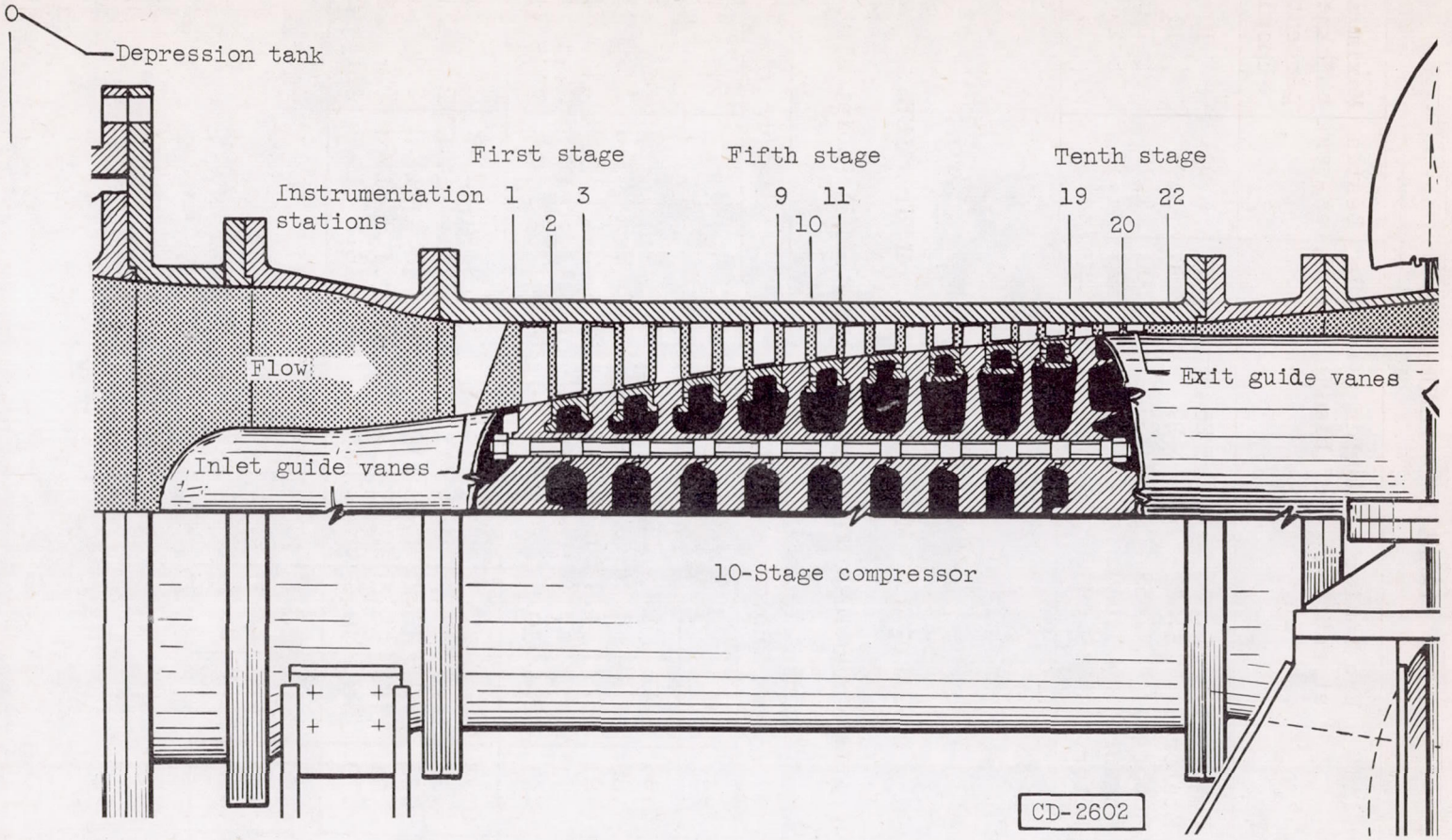

Figure 1. - Schematic diagram of 10-stage compressor showing axial location of instrument measuring stations.

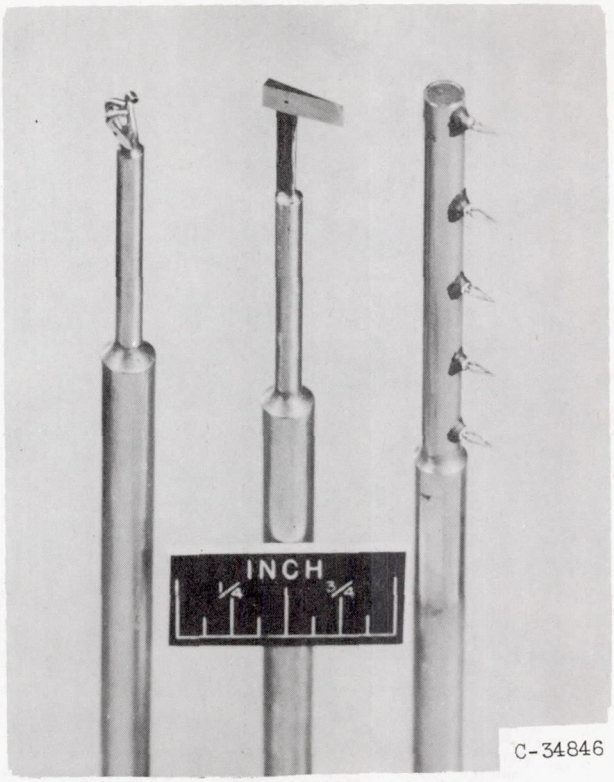

(a) Claw-total-pressure probe. (b) Wedge static-pressure probe. (c) Spike-type radial thermocouple rake.

Figure 2. - Interstage instrumentation.

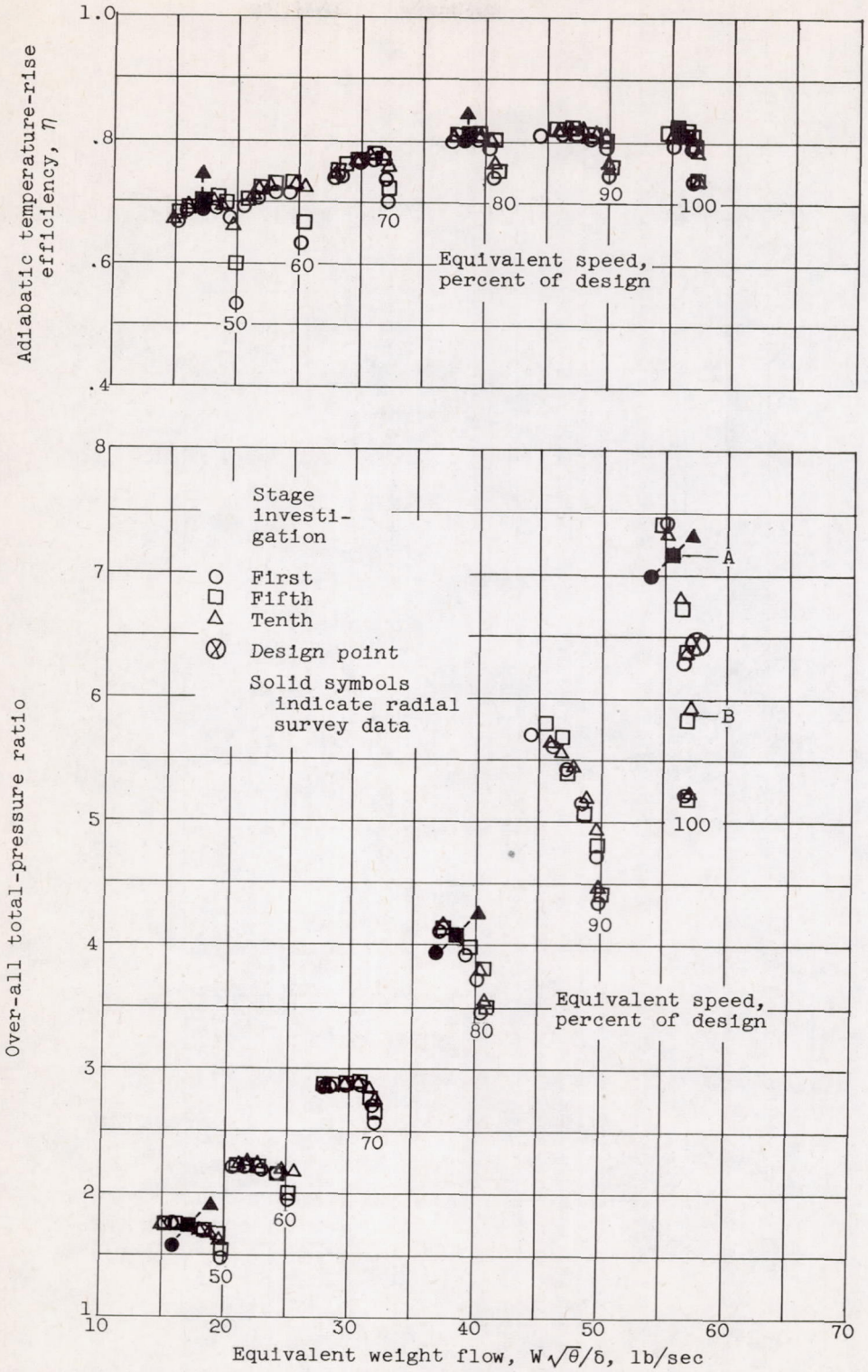

Figure 3. - Over-all compressor performance for three phases of the investigation.

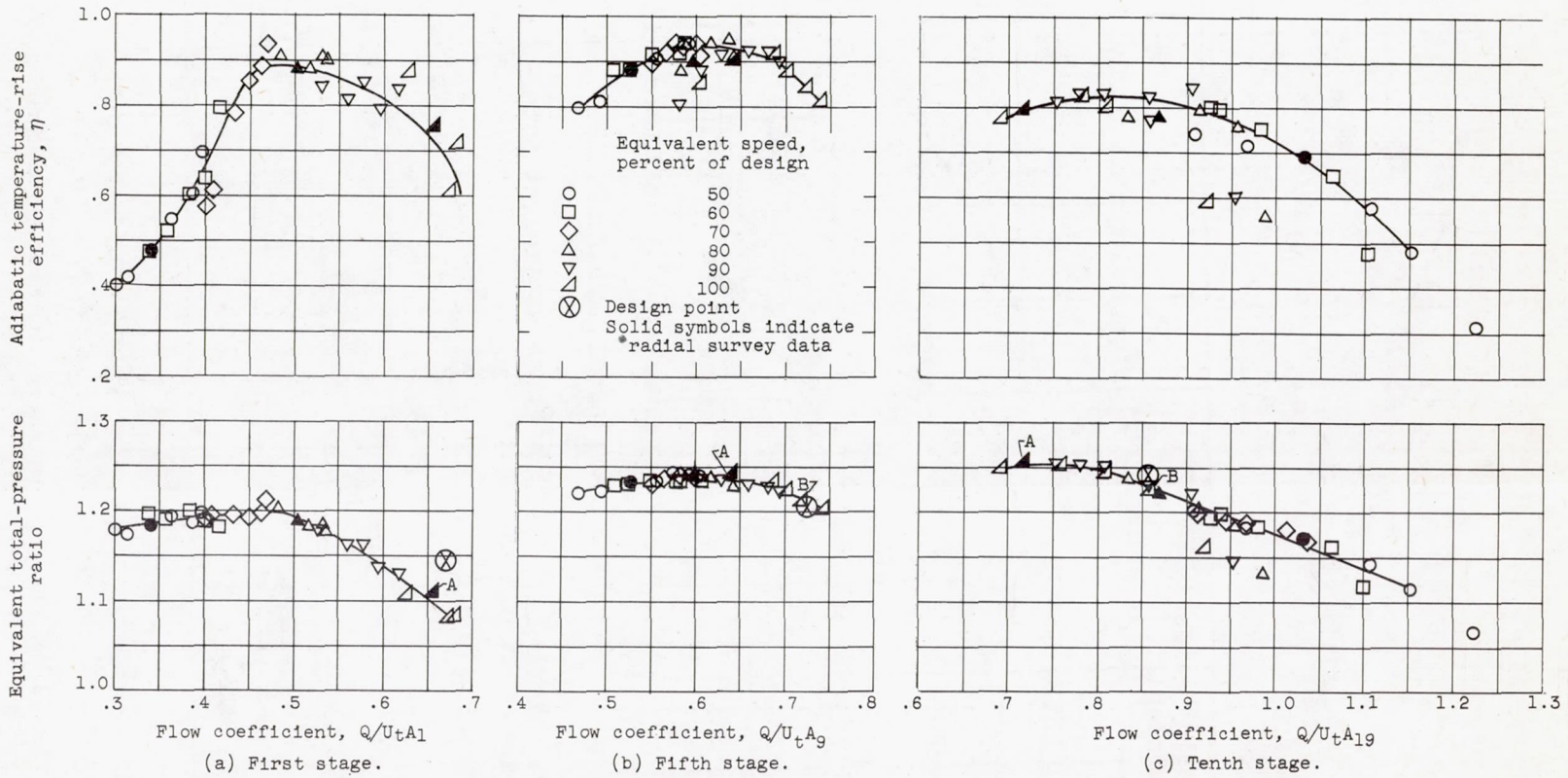

(a) First stage. (b) Fifth stage. (c) Tenth stage.

Figure 4. - Over-all performance of first, fifth, and tenth stages.

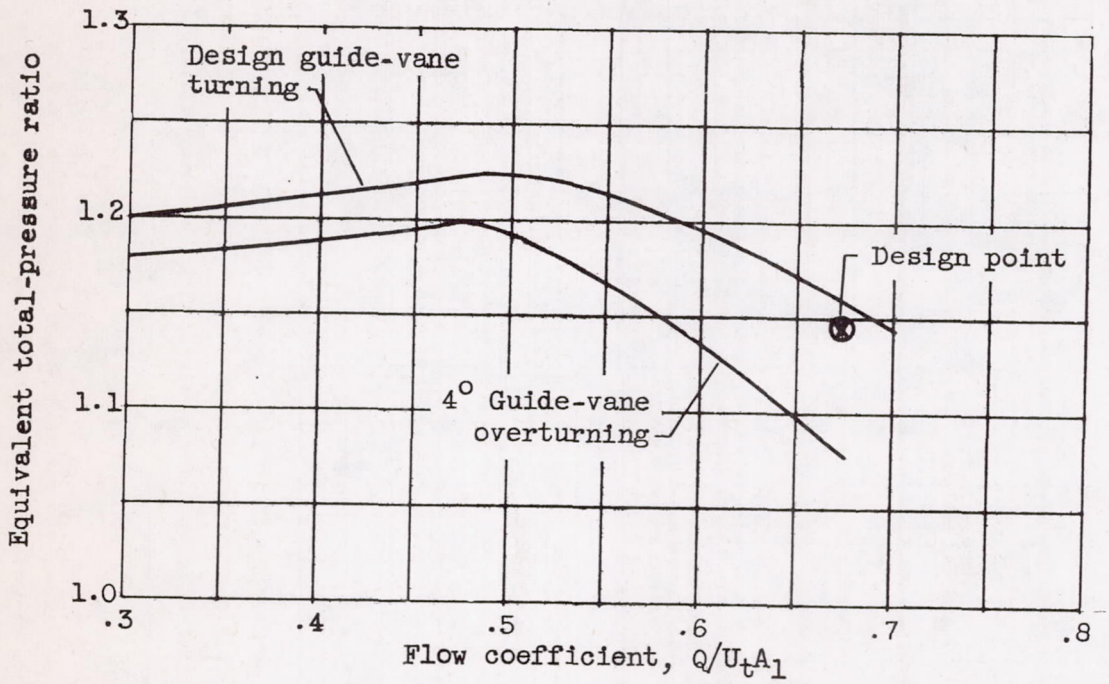

Figure 5. - Variation of first-stage equivalent total-pressure ratio with flow coefficient.

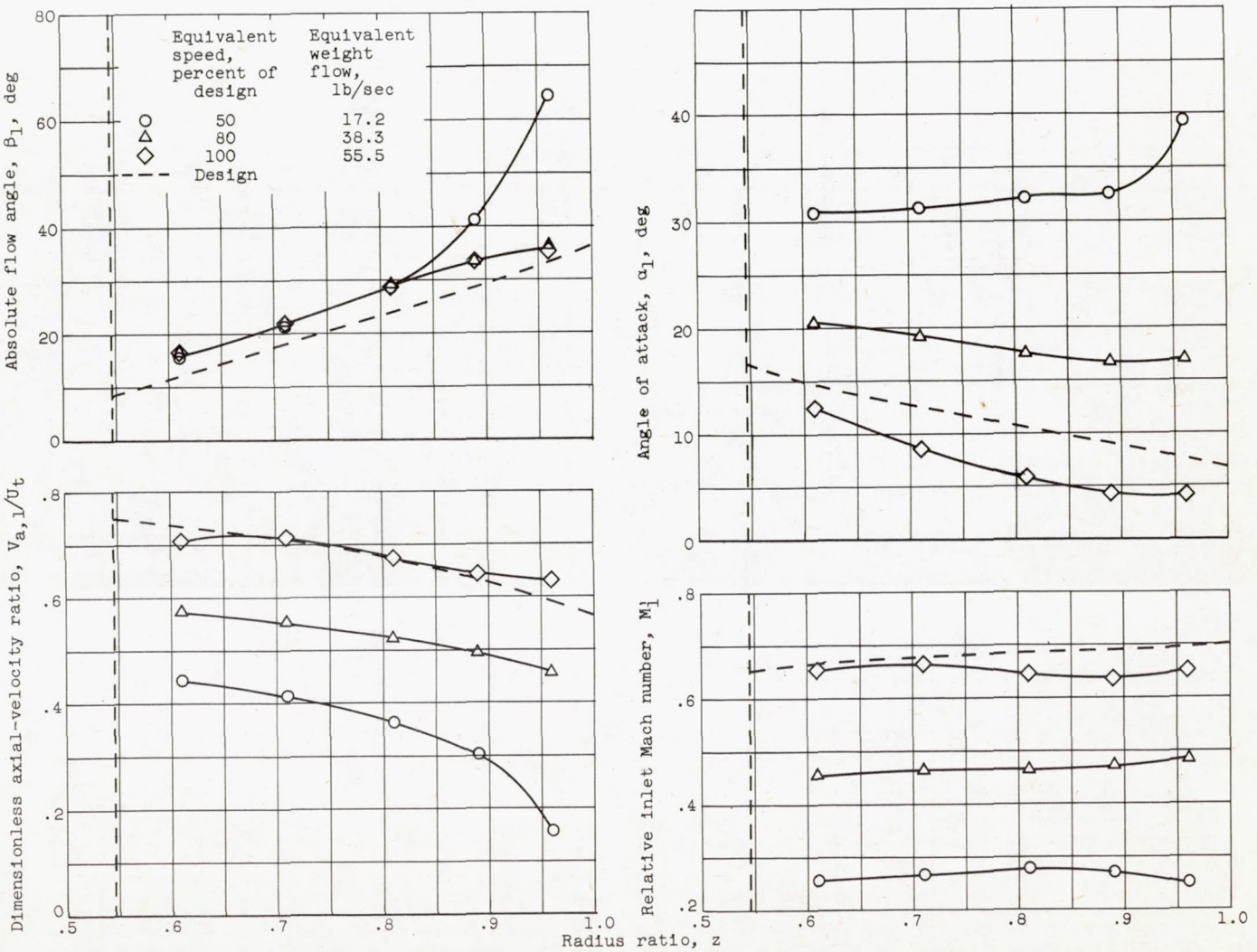

(a) Absolute flow angle and axial-velocity distribution.

(b) Angle of attack and relative inlet Mach number.

Figure 6. - Radial variation of flow conditions entering first rotor row.

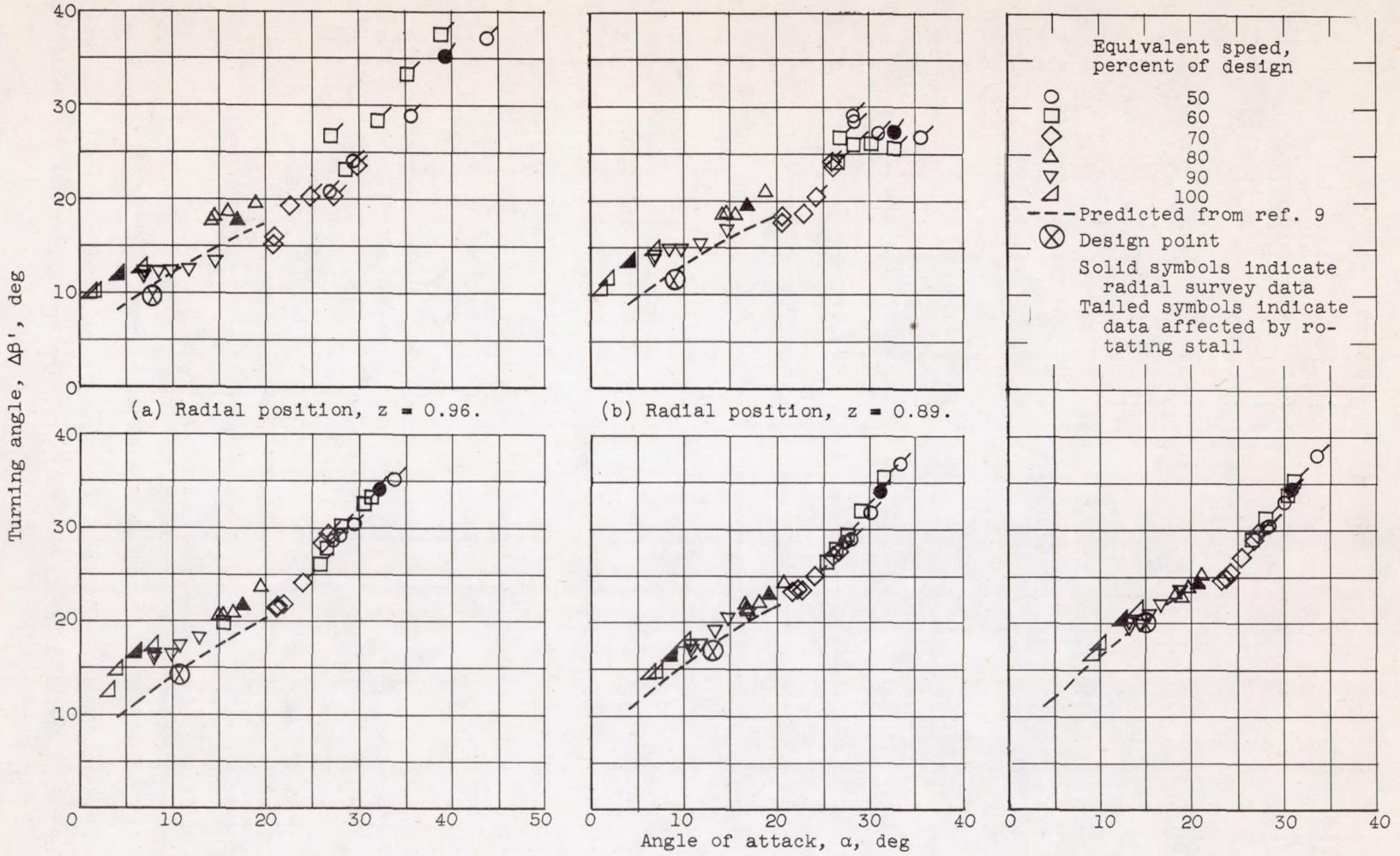

(a) Radial position, z = 0.96.

(b) Radial position, z = 0.89.

(c) Radial position, z = 0.81.

(d) Radial position, z = 0.71.

(e) Radial position, z = 0.61.

Figure 7. - Variation of first-rotor turning angle with angle of attack at five radial positions.

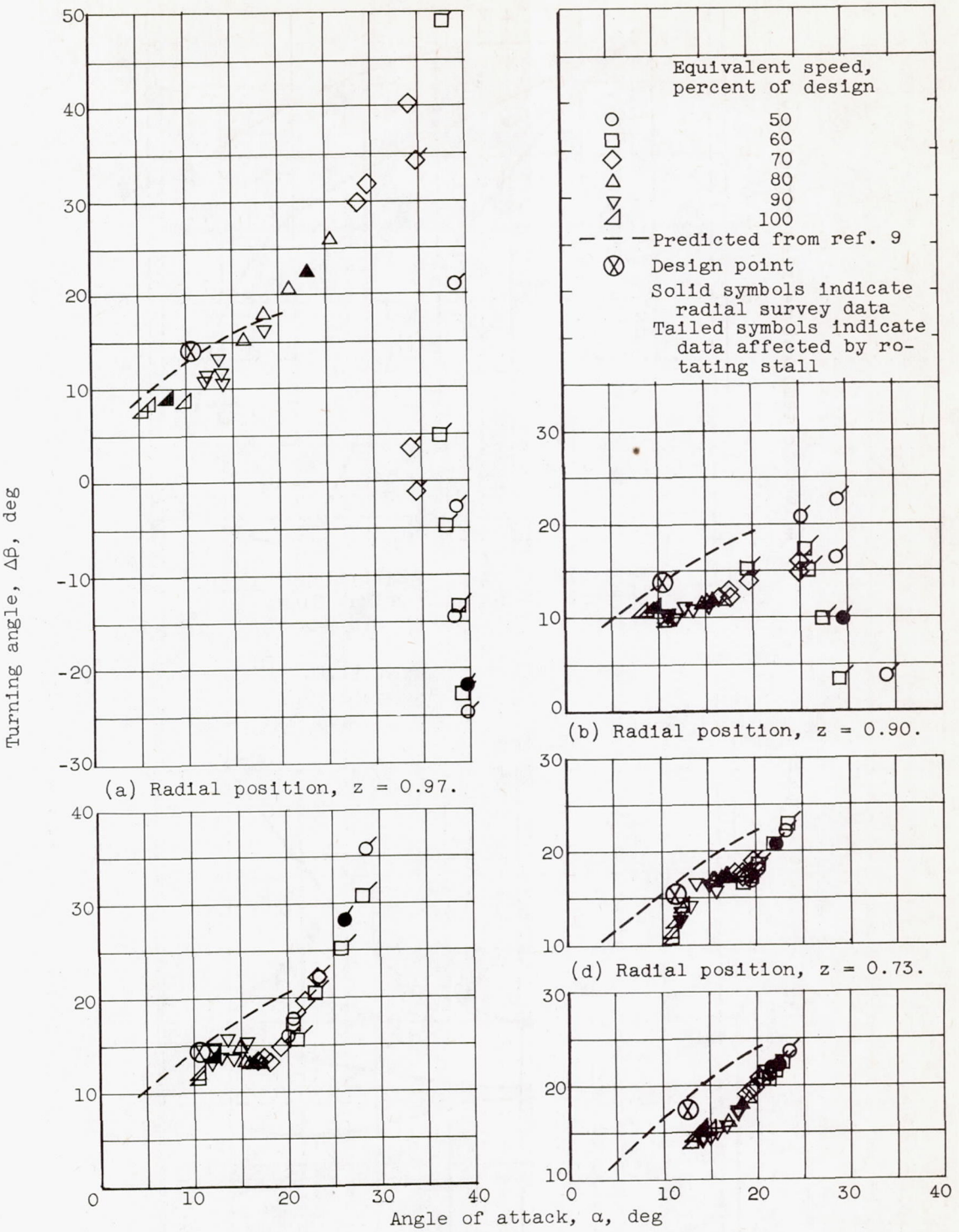

Figure 8. - Variation of first-stator turning angle with angle of attack at five radial positions.

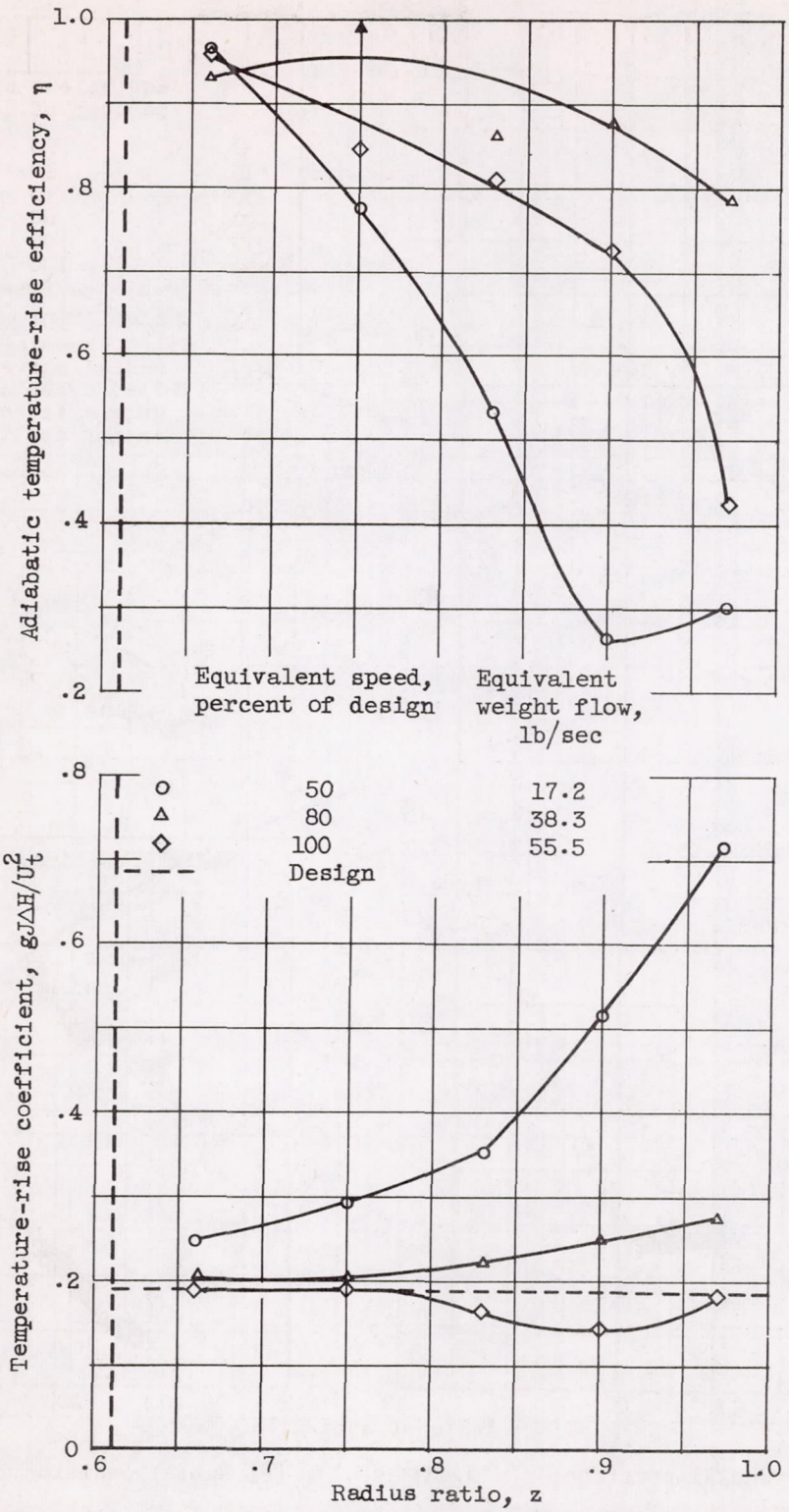

Figure 9. - Radial variation of first-stage performance.

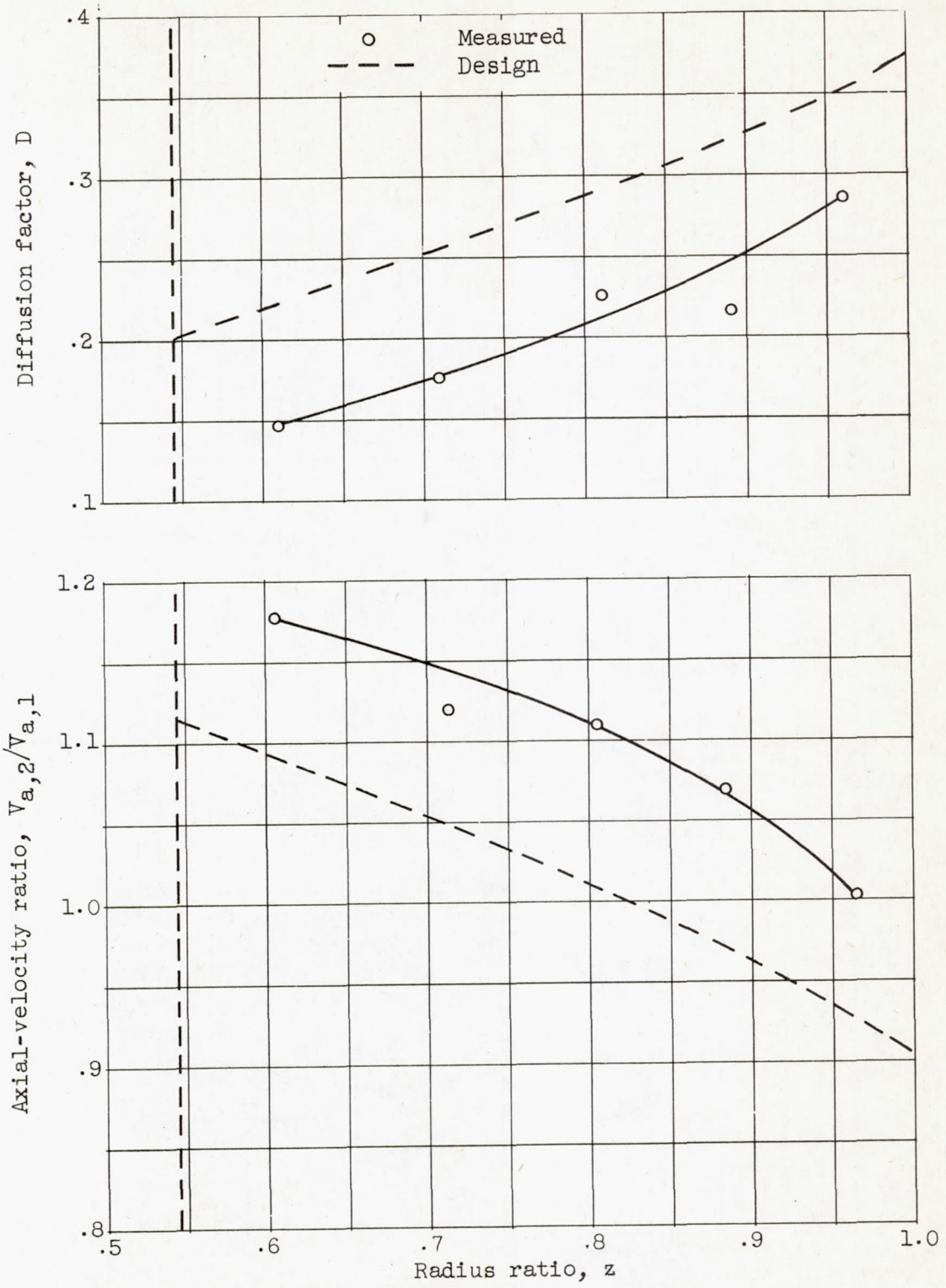

Figure 10. - Radial variation of first-rotor performance at design speed.

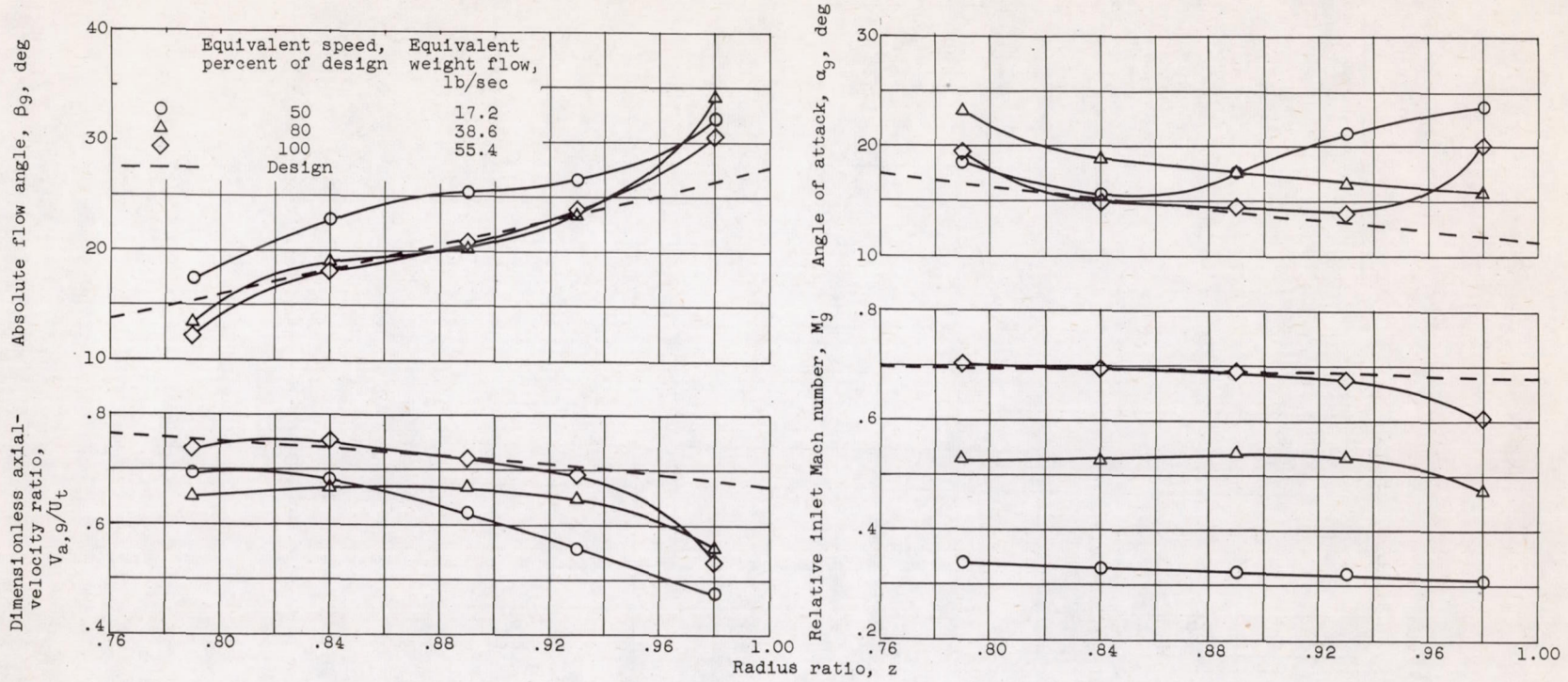

(a) Absolute flow angle and axial-velocity distribution.

(b) Angle of attack and relative inlet Mach number.

Figure 11. - Radial variation of flow conditions entering fifth rotor row.

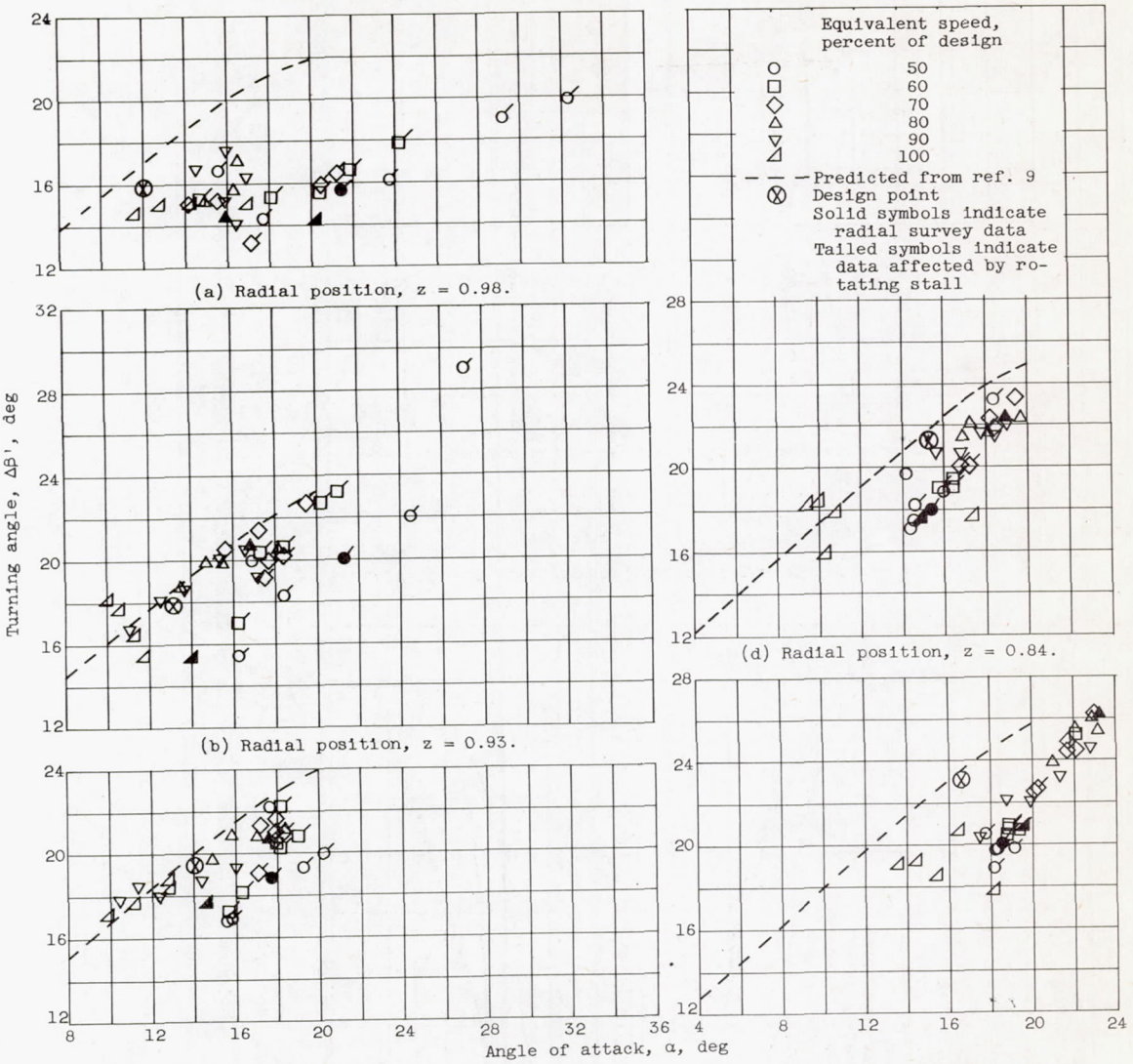

Figure 12. - Variation of fifth-rotor turning angle with angle of attack at five radial positions.

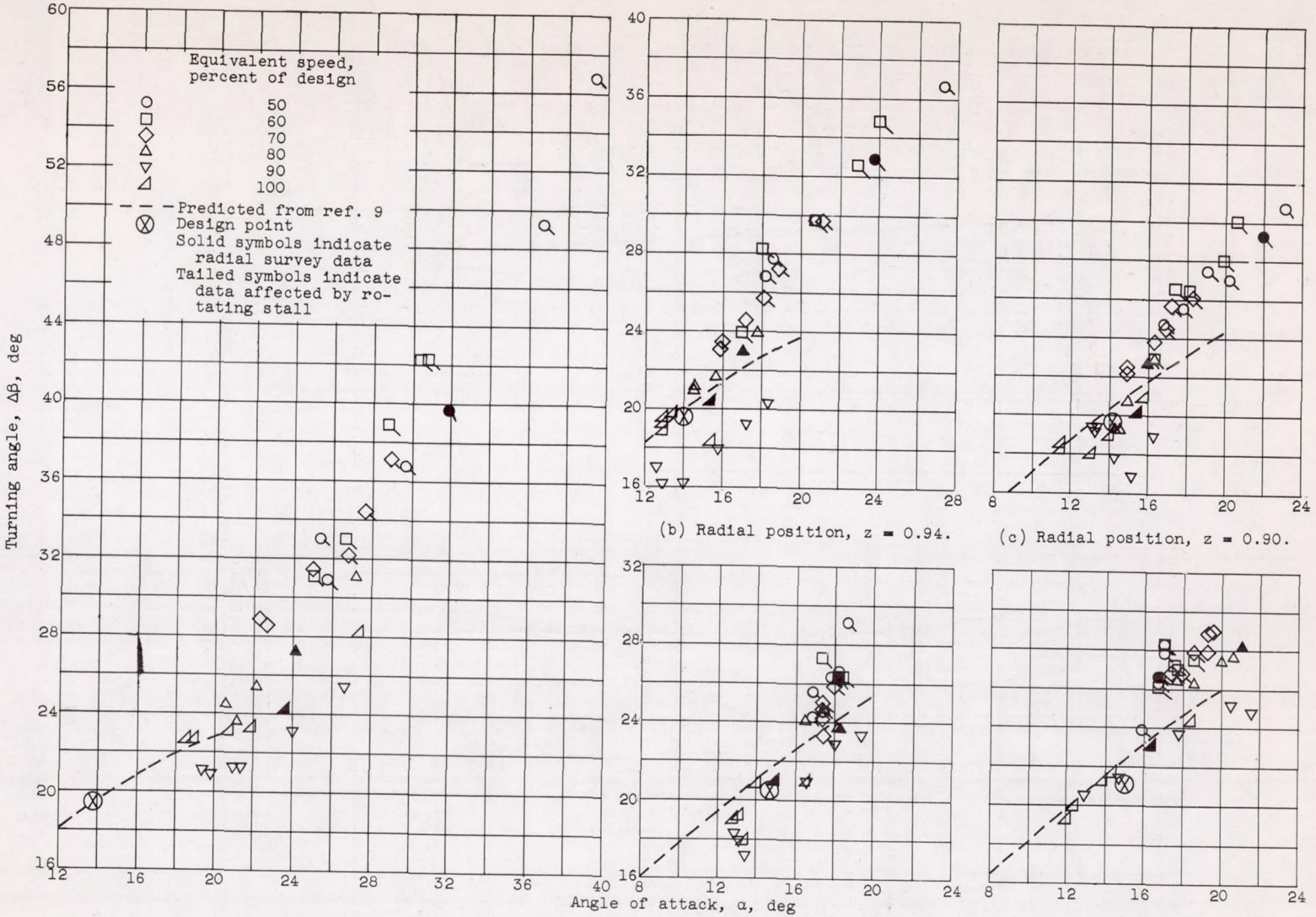

(a) Radial position, z = 0.98.

(b) Radial position, z = 0.94.

(c) Radial position, z = 0.90.

(d) Radial position, z = 0.85.

(e) Radial position, z = 0.81.

Figure 13. - Variation of fifth-stator turning angles with angle of attack at five radial positions.

Figure 14. - Radial variation of fifth-stage performance.

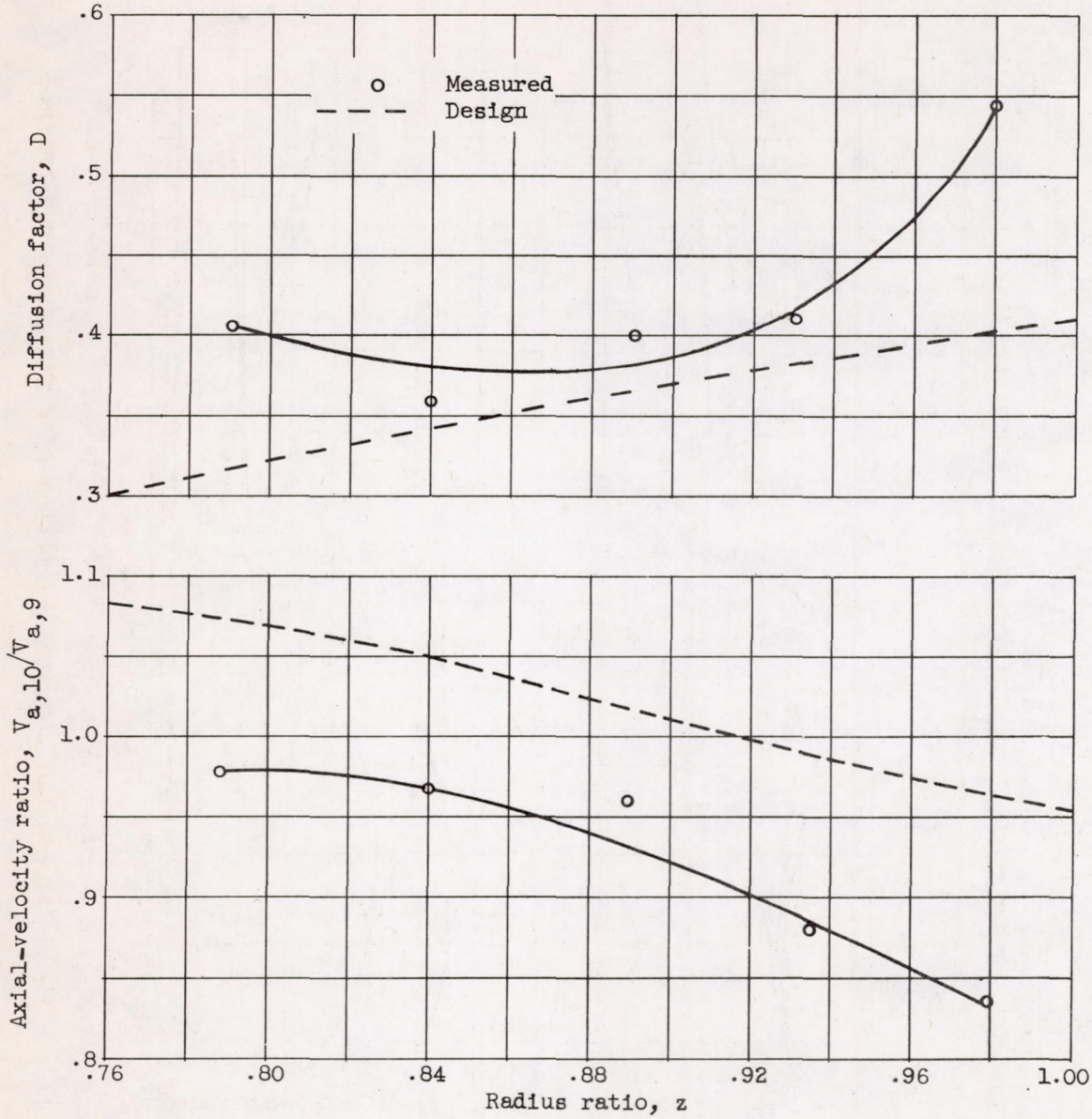

Figure 15. - Radial variation of fifth-rotor performance at design speed.

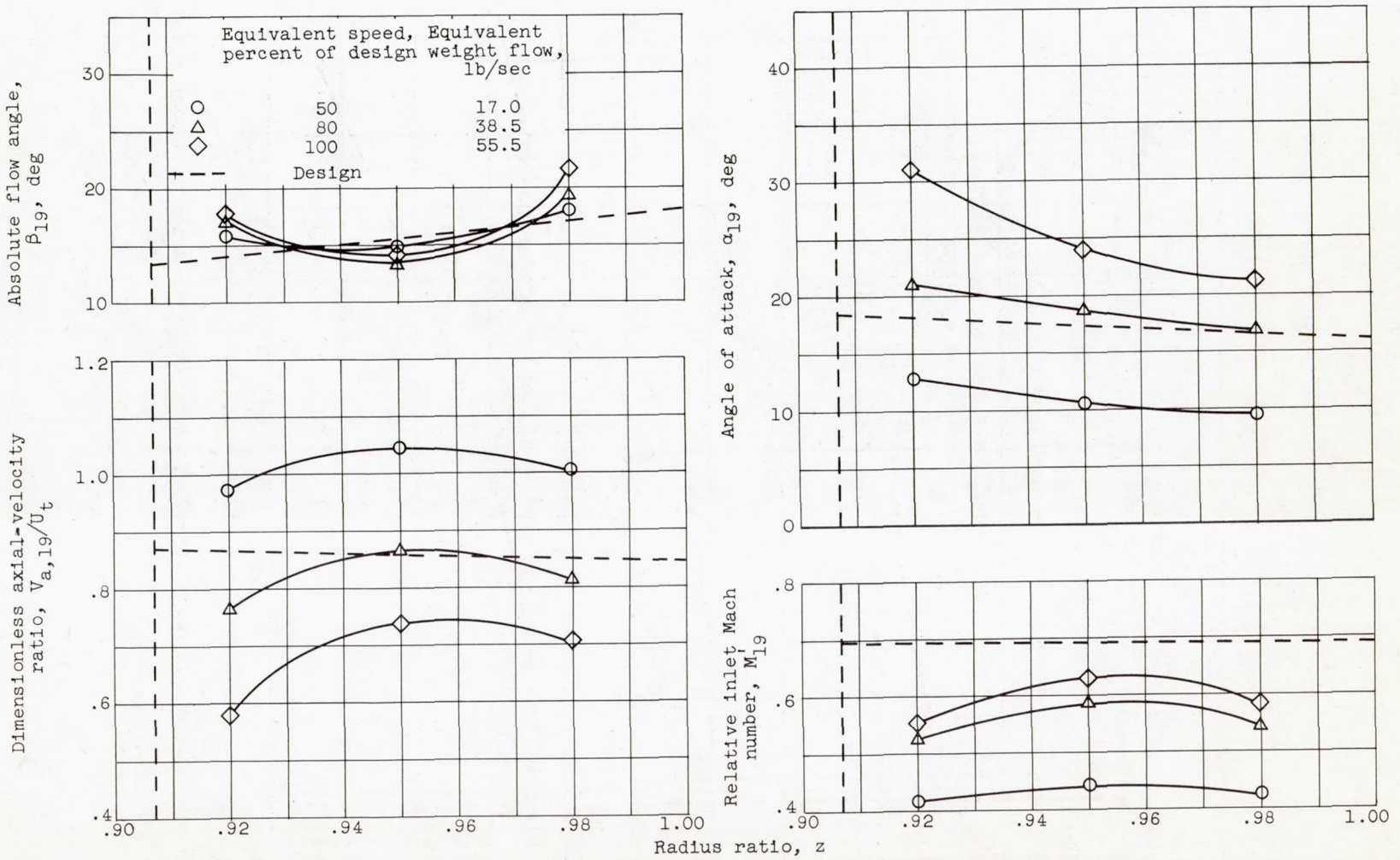

(a) Absolute flow angle and axial-velocity distribution.

(b) Angle of attack and relative inlet Mach number.

Figure 16. - Radial variation of flow conditions entering tenth rotor row.

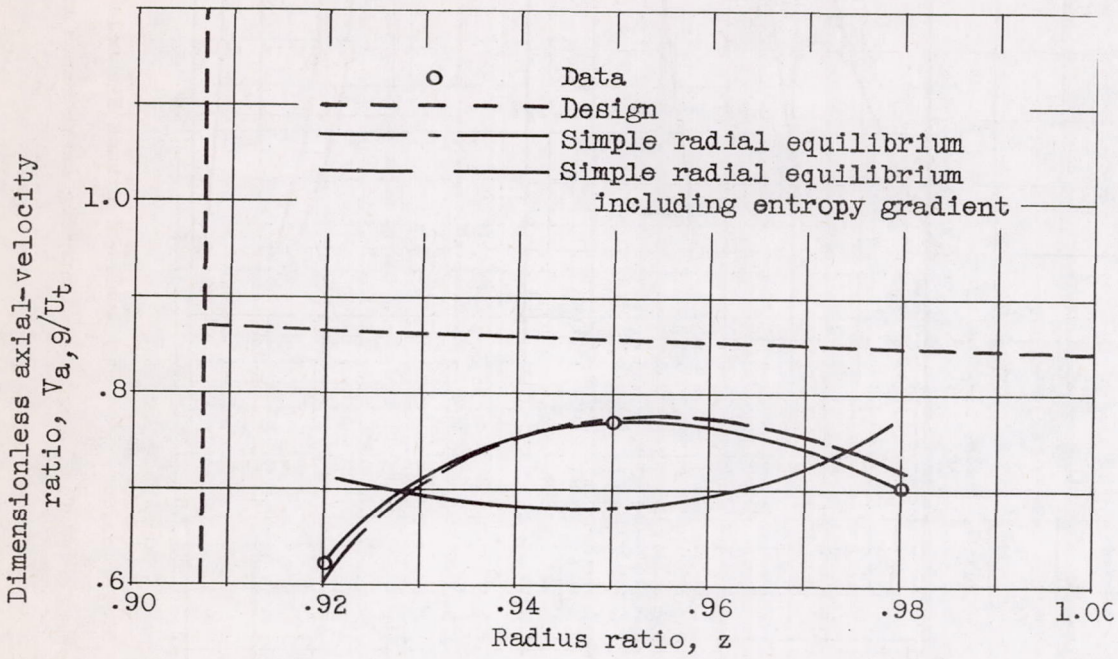

Figure 17. - Simple radial equilibrium comparison of axial-velocity distribution entering tenth rotor.

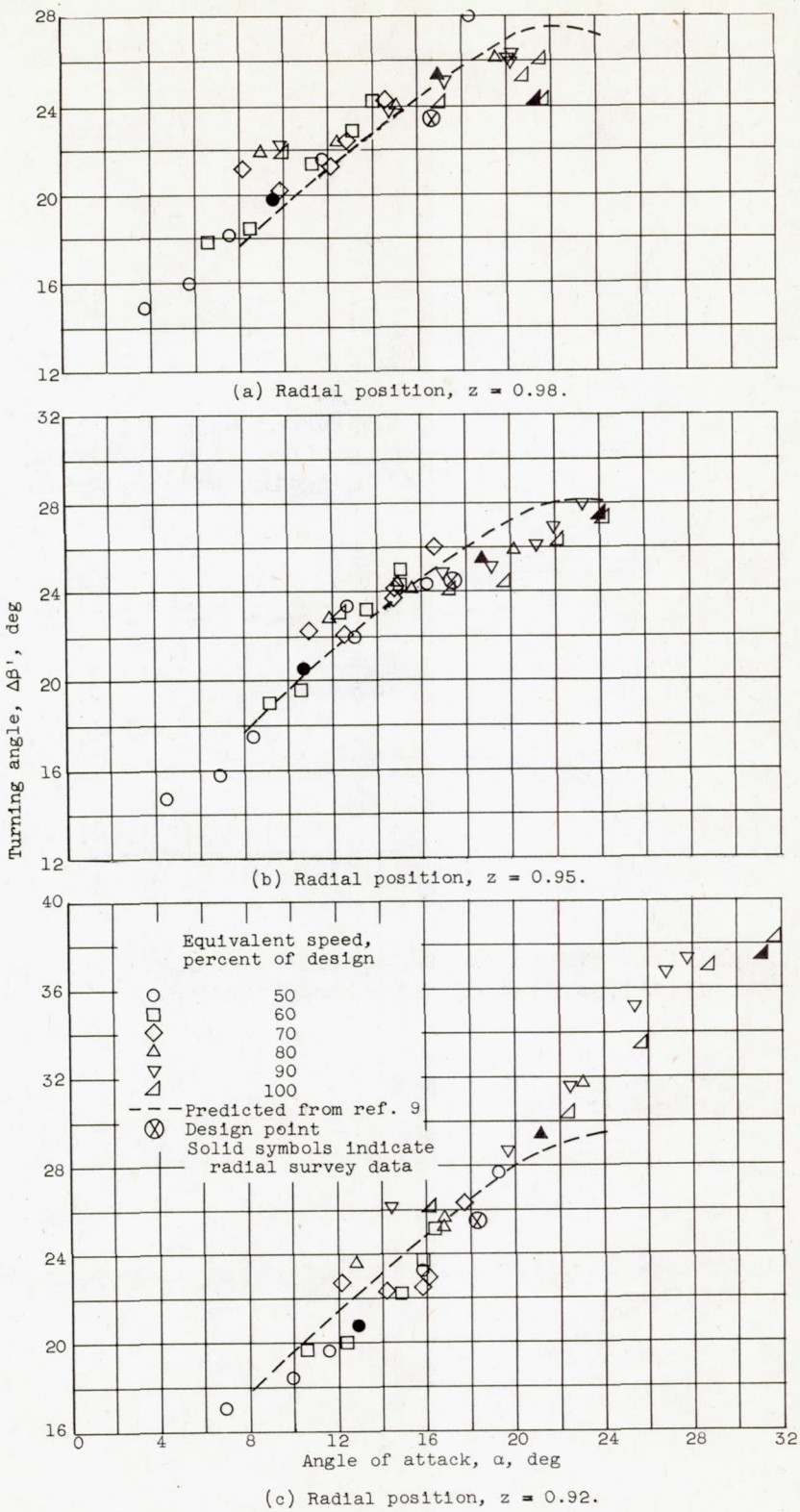

(a) Radial position, z = 0.98.

(b) Radial position, z = 0.95.

(c) Radial position, z = 0.92.

Figure 18. - Variation of tenth-rotor turning angle with angle of attack at three radial positions.

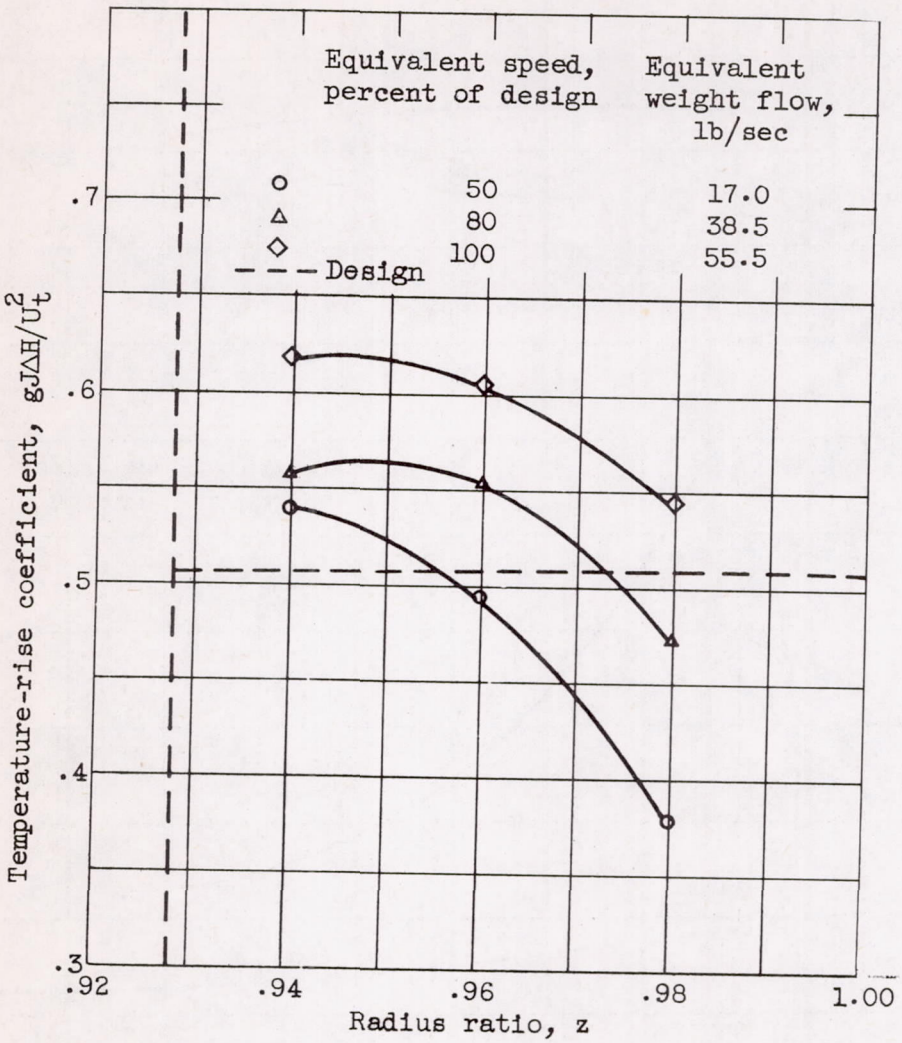

Figure 19. - Radial variation of tenth-stage energy addition.

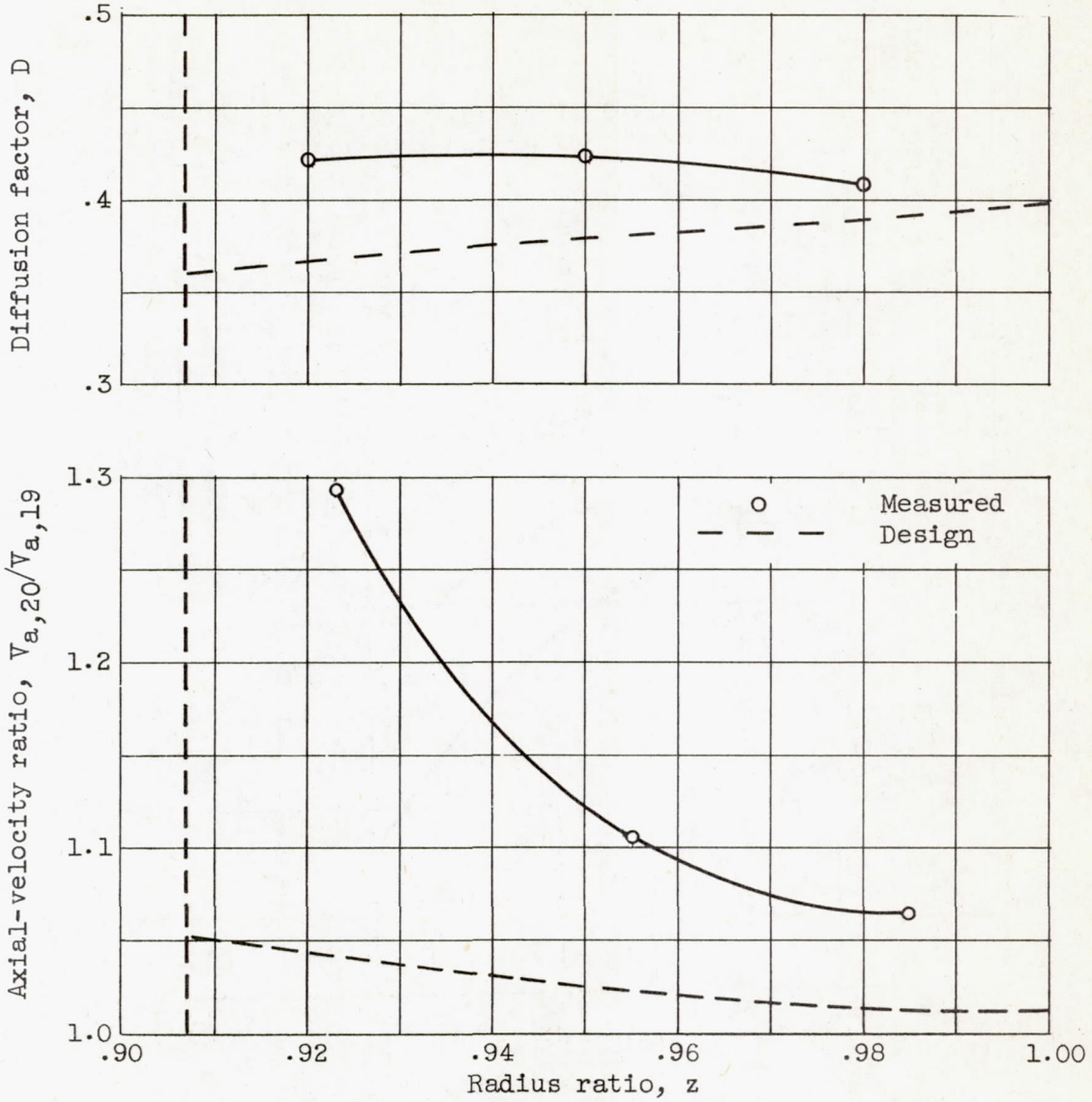

Figure 20. - Radial variation of tenth-rotor performance at design speed.